

Non-LTE abundances of zinc in different spectral type stars and the Galactic $[\text{Zn}/\text{Fe}]$ trend based on quantum-mechanical data on inelastic processes in zinc-hydrogen collisions

T. M. Sitnova^{1*}; S. A. Yakovleva², A. K. Belyaev², L. I. Mashonkina¹

¹*Institute of Astronomy, Russian Academy of Sciences, Pyatnitskaya 48, 119017, Moscow, Russia*

²*Department of Theoretical Physics and Astronomy, Herzen University, St. Petersburg, 191186, Russia*

ABSTRACT

We present a new model atom of Zn I–Zn II based on the most up-to-date photoionisation cross-sections, electron-impact excitation rates, and rate coefficients for the Zn I + H I and Zn II + H[−] collisions. The latter were calculated using the multi-channel quantum asymptotic treatment based on the Born-Oppenheimer approach. Non-LTE analysis was performed for the first time for lines of Zn I and Zn II in the ultraviolet (UV) spectra of two very metal-poor reference stars, HD 84937 and HD 140283. We found consistent non-LTE abundance from the resonance Zn I 2138 Å line, the subordinate lines, and the lines of Zn II. In both stars, non-LTE leads to 0.17 dex higher average abundance from Zn I, while, for Zn II lines, non-LTE corrections are minor and do not exceed 0.06 dex. Using lines of Zn I in the high-resolution spectra, we determined the non-LTE abundances for a sample of 80 stars in the $-2.5 \leq [\text{Fe}/\text{H}] \leq 0.2$ metallicity range. The $[\text{Zn}/\text{Fe}]$ versus $[\text{Fe}/\text{H}]$ diagram reveals a dip, with $[\text{Zn}/\text{Fe}] \simeq 0.3$ in the most metal-poor stars, a close-to-solar value for $[\text{Fe}/\text{H}] \sim -1.2$, and increasing $[\text{Zn}/\text{Fe}]$ up to 0.3 in the thick disk stars. The close-to-solar metallicity stars have subsolar $[\text{Zn}/\text{H}] \simeq -0.1$, on average. Non-LTE abundances of zinc were derived for the first time for seven reference F to B-type stars. We provide a grid of the non-LTE abundance corrections.

Key words: line: formation – stars: atmospheres – stars: abundances.

1 INTRODUCTION

Along with iron, zinc is a pivotal chemical element in astrophysics. It is treated as an iron peak element, however, in contrast to iron, it is volatile and it does not settle in dust grains (Lodders et al. 2009). For this reason, zinc has become a tracer of metallicity in studies of interstellar medium, namely, distant protogalaxies at the early stage of chemical evolution known as damped Ly α systems (DLAs, see, for example, Wolfe et al. 2005; Vladilo et al. 2011; Berg et al. 2016). Studies of gas and dust chemical properties in DLAs with different metallicity invoke the observed Galactic $[\text{Zn}/\text{Fe}]^1 - [\text{Fe}/\text{H}]$ trend. Thus, an accuracy

of zinc abundance determination in low mass long-lived stars with different $[\text{Fe}/\text{H}]$ impacts understanding chemical evolution either in the Milky Way as well as in other distant galaxies.

A lot of studies have been performed to establish $[\text{Zn}/\text{Fe}] - [\text{Fe}/\text{H}]$ Galactic trend (Snedden & Crocker 1988; Sneden et al. 1991; Primas et al. 2000; Mishenina et al. 2002; Reddy et al. 2003; Bensby et al. 2003; Nissen et al. 2004; Chen et al. 2004; Cayrel et al. 2004; Bensby et al. 2005; Takeda et al. 2005; Saito et al. 2009; Bensby et al. 2014; Duffau et al. 2017; Mikolaitis et al. 2017; Roederer & Barklem 2018). The majority of the above studies report on a moderate overabundance in $[\text{Zn}/\text{Fe}]$ in stars with $[\text{Fe}/\text{H}] < -1$ and decreasing $[\text{Zn}/\text{Fe}]$ at higher metallicity. Some studies managed to detect a separation and higher $[\text{Zn}/\text{Fe}]$ in thick disk stars compared to thin disk stars with similar $[\text{Fe}/\text{H}]$ (Bensby et al. 2003; Mikolaitis et al. 2017). Such a behaviour is qualitatively

* E-mail: sitnova@inasan.ru

¹ We use a standard designation, $[X/Y] = \log(N_X/N_Y)_* - \log(N_X/N_Y)_\odot$, where N_X and N_Y are total number densities of element X and Y, respectively.

similar to those observed for α -elements. Other details in the zinc trend were figured out: Mishenina et al. (2002), Nissen et al. (2004), and Saito et al. (2009) found a pit in $[\text{Zn}/\text{Fe}]$ at $[\text{Fe}/\text{H}] \simeq -1.2$. At solar $[\text{Fe}/\text{H}]$, Duffau et al. (2017) found lower $[\text{Zn}/\text{Fe}]$ ratios in stars at Galactocentric distances less than 7.5 kpc. What for very metal-poor (VMP, $[\text{Fe}/\text{H}] < -2$) tail of the trend, $[\text{Zn}/\text{Fe}]$ increases with decreasing metallicity $[\text{Fe}/\text{H}] < -2.5$ and can reach $[\text{Zn}/\text{Fe}] = 1$ dex at $[\text{Fe}/\text{H}] = -4$ (Primas et al. 2000; Cayrel et al. 2004; Takeda et al. 2005).

Zinc abundance determination in the above studies rely on the assumption of local thermodynamic equilibrium (LTE). An exception is Takeda et al. (2005, hereafter, T05) and Takeda et al. (2016), who studied an impact of non-LTE effects on Zn I 4722, 4810, and 6362 Å lines in a wide metallicity range of late type stars. T05 found non-LTE abundance corrections (Δ_{NLTE} , the difference between non-LTE and LTE abundances for individual spectral lines) to be moderate in absolute value, within 0.1 dex. However, the value and sign of non-LTE corrections depend on stellar parameters and metallicity. For example, for the Zn I 4810 Å line in the Sun, T05 found $\Delta_{\text{NLTE}} = -0.05$, while, for metal-poor stars, non-LTE abundance corrections are mainly positive. Thus, neglecting the non-LTE effects may lead to a shift in $[\text{Zn}/\text{H}]$ ratio of 0.15 dex and distort $[\text{Zn}/\text{Fe}] - [\text{Fe}/\text{H}]$ abundance trend.

Not only accurate line formation, but also an accurate homogeneous set of stellar atmosphere parameters (effective temperature, surface gravity, and metallicity) are required to establish a robust $[\text{El}/\text{Fe}]$ trend. T05 compiled equivalent width measurements and stellar atmosphere parameters from different studies, determined by different methods. For example, Cayrel et al. (2004) determined surface gravities for a sample of metal-poor stars using Fe I-Fe II and Ti I-Ti II ionisation balance in LTE, while Nissen et al. (2004) adopted distance based surface gravities. While, in solar type dwarfs, non-LTE weakly affect Fe I-Fe II and Ti I-Ti II abundance difference, in metal-poor stars, non-LTE effects are significant for lines of neutral species, and an application of ionisation balance method based on LTE analysis may lead to uncertainty in surface gravity of 0.5 dex in dwarfs (see, for example, Sitnova et al. 2015) and to even larger effects in giants (see, for example, Mashonkina et al. 2011). Adopting stellar parameters determined by different methods can produce a systematic offset between abundances from different stellar subsamples.

At metallicity $[\text{Fe}/\text{H}] < -3$, Zn I lines in the visible spectrum range (4680, 4722, 4810, and 6362 Å) became weaker and hardly can be detected. To determine zinc abundance in stars with extremely low metallicities, one have to invoke the Zn I and Zn II resonance line observed in the ultraviolet spectrum (UV) range (Roederer et al. 2016; Roederer & Barklem 2018; Ezzeddine et al. 2019). For six metal-poor stars ($-2.5 < [\text{Fe}/\text{H}] < -1$), Roederer & Barklem (2018) found a good agreement between the average abundance from Zn I lines in the visible and UV range and the resonance Zn II 2062 Å line. Roederer & Barklem (2018) reported significant abundance uncertainties of 0.2 dex for the UV lines, and, in metal-poor reference stars with well-determined stellar parameters, abundances between different Zn I lines differ up to 0.22 dex. In order to safely adopt these lines for abun-

dance determinations in extremely MP stars, accurate line formation calculations should be performed.

Lines of Zn I are observed also in the visible spectrum range in A and late B-type stars. With the ionisation energy $E_{\text{ion}}(\text{Zn I}) = 9.39$ eV, in AB-type stars, Zn I is a minority species and one can expect significant non-LTE effects. To our knowledge, the non-LTE calculations have not been performed yet for zinc in hot stars. To estimate an impact of non-LTE on abundance determination detailed calculations are required.

We constructed the Zn I-II model atom using the most accurate atomic data for electronic collisions, collisions with hydrogen atoms, and photoionisation cross-section. The method of non-LTE abundance determination, atomic data, and codes are described in Sect. 2. The mechanism of the departures from LTE are described in Sect. 3. We tested the non-LTE method for zinc by analysis of different Zn I and Zn II lines in reference stars (Sect. 4). Non-LTE abundances of zinc were derived for seven F to late B-type stars (Sect. 5). Using a sample of dwarf stars in a wide metallicity range and robust stellar parameters, we revisited the Galactic $[\text{Zn}/\text{Fe}] - [\text{Fe}/\text{H}]$ trend (Sect. 6). To account for the departures from LTE, we provide non-LTE abundance corrections for different zinc lines (Sect. 7). Our results are summarised in Sect. 8.

2 ABUNDANCE DETERMINATION METHOD

2.1 Model atom

Energy levels. Our Zn I-II model atom (Fig. 1) includes 28 levels of Zn I, 7 levels of Zn II, and the ground state of Zn III. The list of energy levels and transitions is taken from R. Kurucz webpage². For the atomic levels with E_{exc} up to 9 eV their energies are taken from the laboratory measurements and implemented in the atomic structure calculations by R. Kurucz. For Zn I, we included into the model atom all levels up to the ionization threshold, 9.39 eV. Levels with an excitation energy larger than 8.2 eV are combined into the superlevels with energy separation of 0.1 eV. Fine structure is neglected for Zn I. Zn II model atom includes seven levels with the excitation energy up to 12.6 eV. For $4p\ ^2P^\circ$ level, we take into account fine structure, since the splitting is significant and amounts to 0.11 eV.

Radiative transitions. The atomic levels in the model atom are connected by radiative and collisional bound-bound and bound-free transitions. In the statistical equilibrium (SE) calculations, the oscillator strength are taken from R. Kurucz database. For strong transitions that correspond to the observed in stellar spectra lines, we adopted in SE calculations the oscillator strengths from laboratory measurements of Abjean (1975) and Roederer & Lawler (2012) for Zn I, and from Mayo et al. (2006) for Zn II. For accurate calculation of radiative rates in the resonance transitions of Zn I and Zn II, we use the Voigt profile and a fine wavelength mesh, which fully covers the lines core and wings.

For Zn I terms with $E_{\text{exc}} \leq 8.2$ eV, we use photoionisation cross-sections from the R-matrix calculations of Liu et al. (2011). For the remaining high-excitation levels,

² <http://kurucz.harvard.edu/atoms.html>

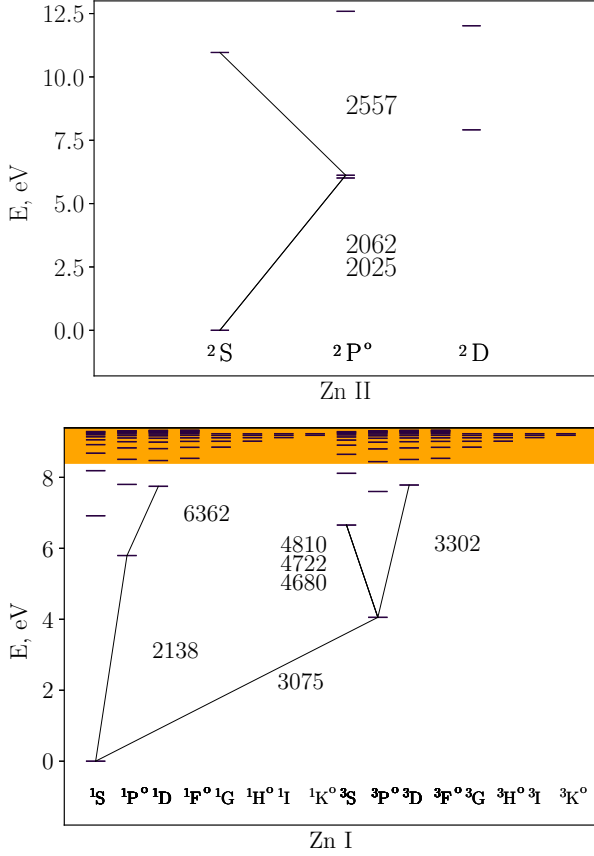


Figure 1. Zn I (bottom panel) and Zn II (top panel) grotrian diagrams. The high-excitation levels of Zn I marked with shaded area are combined into the seventeen superlevels. The wavelengths of the observed spectral lines are indicated in Å.

we assume a hydrogenic approximation with using an effective principle quantum number. We compare the quantum mechanical photoionisation cross-sections with the hydrogenic ones for selected levels Zn I in Fig. 2.

For all levels of Zn II, we calculated photoionization cross-sections using hydrogenic approximation with the effective principle quantum number. Zn II is a majority species in the stellar parameter range with which we concern. Therefore, the ionisation / recombination processes nearly do not affect the SE of Zn II.

Collisions with electrons. For electronic collisions of Zn I, we used the cross sections generated in the R-matrix calculations described by Zatsarinny & Bartschat (2005). These calculations were performed for ten transitions from the ground state of Zn I to the levels up to $6s^1S$ with $E_{exc} = 8.2$ eV. The rate coefficients were computed by integrating the cross-sections over the Maxwellian velocity distribution for electrons, and they are presented in Table 1. For the ten transitions, Fig. 3 shows a comparison of electron-impact excitation rates derived from Zatsarinny & Bartschat (2005) data and those calculated with the approximate van Regemorter (1962) and Woolley & Allen (1948) formulae, for radiatively allowed and forbidden transitions, respectively. The above approximate formulae were adopted for electron collision rates calculations for the remaining Zn I and Zn II transitions. Elec-

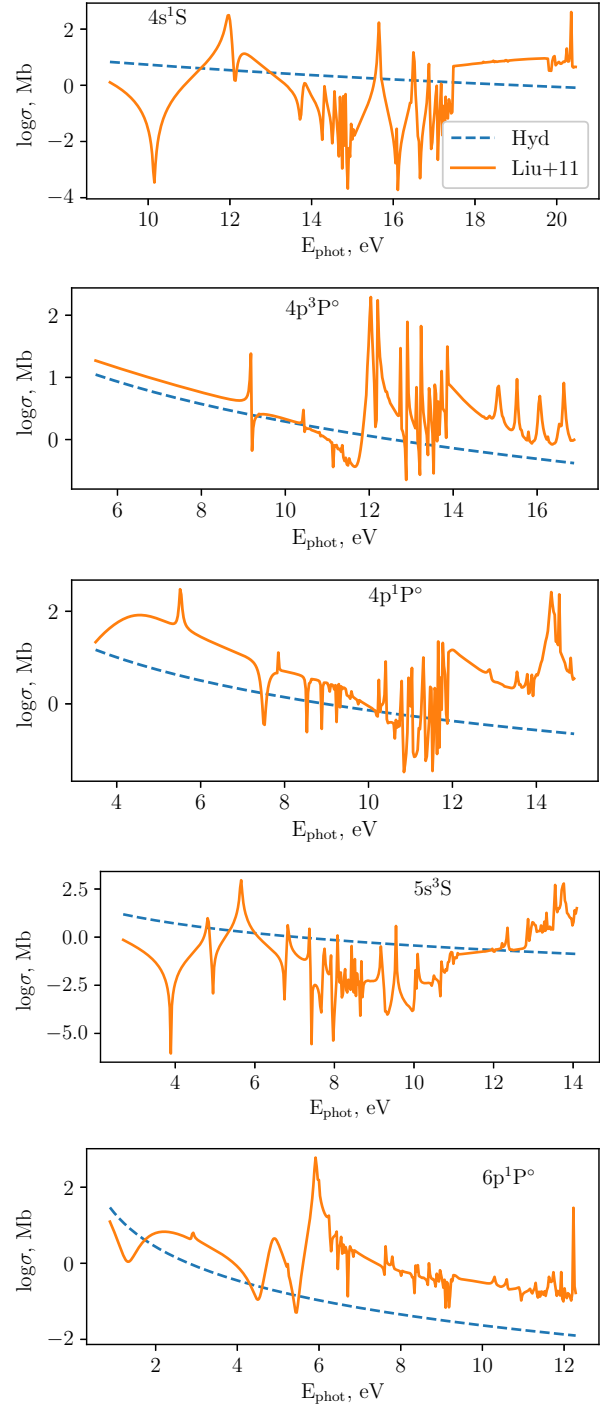


Figure 2. Photoionisation cross-sections for the selected levels of Zn I from quantum mechanical calculations of Liu et al. (2011, solid lines) and computed in the hydrogenic approximation (dashed lines).

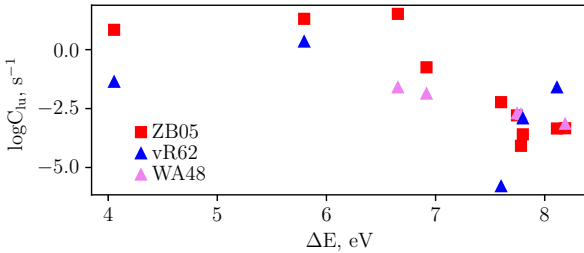
tron impact ionisation is calculated with the Seaton (1962) formula.

Collisions with hydrogen atoms.

For SE calculations of Zn I in late-type stars, inelastic processes in collisions with H I atoms are taken into account. We have calculated for the first time the rate coefficients for bound-bound transitions in inelastic collisions of zinc

Table 1. Electron-impact excitation rate coefficients (in $\text{cm}^3 \text{s}^{-1}$) for the ZnI transitions at the temperatures from 2000 K to 50000 K with a step of 2000 K.

4s ^1S – 4p $^3\text{P}^\circ$										
0.7713E-17	0.9732E-12	0.4484E-10	0.2891E-09	0.8547E-09	0.1718E-08	0.2776E-08	0.3922E-08	0.5071E-08	0.6167E-08	
0.7178E-08	0.8088E-08	0.8892E-08	0.9591E-08	0.1019E-07	0.1070E-07	0.1113E-07	0.1148E-07	0.1177E-07	0.1199E-07	
0.1217E-07	0.1230E-07	0.1239E-07	0.1245E-07	0.1247E-07						
4s ^1S – 4p $^1\text{P}^\circ$										
0.2192E-16	0.2832E-11	0.1316E-09	0.8526E-09	0.2528E-08	0.5091E-08	0.8239E-08	0.1165E-07	0.1508E-07	0.1835E-07	
0.2137E-07	0.2409E-07	0.2650E-07	0.2859E-07	0.3040E-07	0.3193E-07	0.3321E-07	0.3427E-07	0.3513E-07	0.3581E-07	
0.3634E-07	0.3674E-07	0.3701E-07	0.3718E-07	0.3727E-07						
4s ^1S – 5s ^3S										
0.3423E-16	0.4570E-11	0.2147E-09	0.1398E-08	0.4157E-08	0.8388E-08	0.1359E-07	0.1925E-07	0.2493E-07	0.3036E-07	
0.3537E-07	0.3990E-07	0.4390E-07	0.4739E-07	0.5039E-07	0.5294E-07	0.5507E-07	0.5684E-07	0.5828E-07	0.5942E-07	
0.6031E-07	0.6097E-07	0.6144E-07	0.6173E-07	0.6188E-07						
4s ^1S – 5s ^1S										
0.5053E-21	0.9998E-14	0.2888E-11	0.5077E-10	0.2895E-09	0.9379E-09	0.2194E-08	0.4181E-08	0.6934E-08	0.1042E-07	
0.1454E-07	0.1919E-07	0.2424E-07	0.2955E-07	0.3502E-07	0.4053E-07	0.4600E-07	0.5136E-07	0.5654E-07	0.6151E-07	
0.6624E-07	0.7070E-07	0.7489E-07	0.7879E-07	0.8240E-07						
4s ^1S – 5p $^3\text{P}^\circ$										
0.9700E-24	0.2377E-15	0.1340E-12	0.2994E-11	0.1858E-10	0.6122E-10	0.1409E-09	0.2599E-09	0.4141E-09	0.5961E-09	
0.7975E-09	0.1010E-08	0.1227E-08	0.1443E-08	0.1654E-08	0.1856E-08	0.2048E-08	0.2227E-08	0.2394E-08	0.2548E-08	
0.2688E-08	0.2816E-08	0.2931E-08	0.3034E-08	0.3127E-08						
4s ^1S – 4d ^1D										
0.9185E-25	0.5545E-16	0.4341E-13	0.1178E-11	0.8464E-11	0.3149E-10	0.8066E-10	0.1637E-09	0.2841E-09	0.4419E-09	
0.6338E-09	0.8549E-09	0.1099E-08	0.1360E-08	0.1632E-08	0.1910E-08	0.2189E-08	0.2464E-08	0.2733E-08	0.2994E-08	
0.3244E-08	0.3481E-08	0.3706E-08	0.3917E-08	0.4115E-08						
4s ^1S – 4d ^3D										
0.9982E-27	0.2279E-17	0.2746E-14	0.9187E-13	0.7412E-12	0.2950E-11	0.7853E-11	0.1627E-10	0.2853E-10	0.4451E-10	
0.6378E-10	0.8574E-10	0.1097E-09	0.1351E-09	0.1612E-09	0.1876E-09	0.2138E-09	0.2396E-09	0.2645E-09	0.2884E-09	
0.3112E-09	0.3327E-09	0.3529E-09	0.3718E-09	0.3894E-09						
4s ^1S – 5p $^1\text{P}^\circ$										
0.3046E-26	0.7014E-17	0.8458E-14	0.2826E-12	0.2276E-11	0.9041E-11	0.2403E-10	0.4971E-10	0.8706E-10	0.1357E-09	
0.1942E-09	0.2609E-09	0.3336E-09	0.4105E-09	0.4897E-09	0.5696E-09	0.6489E-09	0.7267E-09	0.8020E-09	0.8742E-09	
0.9430E-09	0.1008E-08	0.1069E-08	0.1126E-08	0.1179E-08						
4s ^1S – 6s ^3S										
0.5336E-26	0.1240E-16	0.1492E-13	0.4965E-12	0.3979E-11	0.1574E-10	0.4165E-10	0.8587E-10	0.1499E-09	0.2330E-09	
0.3328E-09	0.4461E-09	0.5695E-09	0.6997E-09	0.8335E-09	0.9684E-09	0.1102E-08	0.1233E-08	0.1360E-08	0.1481E-08	
0.1597E-08	0.1706E-08	0.1808E-08	0.1904E-08	0.1992E-08						
4s ^1S – 6s ^1S										
0.2987E-26	0.1139E-16	0.1704E-13	0.6606E-12	0.6011E-11	0.2656E-10	0.7759E-10	0.1746E-09	0.3294E-09	0.5485E-09	
0.8326E-09	0.1178E-08	0.1577E-08	0.2022E-08	0.2502E-08	0.3006E-08	0.3527E-08	0.4055E-08	0.4583E-08	0.5105E-08	
0.5615E-08	0.6110E-08	0.6587E-08	0.7043E-08	0.7477E-08						

**Figure 3.** Electron-impact excitation rates for the ZnI transitions at $T = 5000 \text{ K}$ and $N_e = 1.05 \times 10^{12}$ (these values correspond to $\log T_{5000} = -1$ in model atmosphere with $T_{\text{eff}} / \log g / [\text{Fe}/\text{H}] = 5780/3.70/-2.46$) calculated from Zatsarinny & Bartschat (2005) data (squares) and formulae of van Regemorter (1962) and Woolley & Allen (1948) (blue and violet triangles, respectively).

atoms and positive ions with hydrogen atoms and negative ions. The calculations are performed using the multichannel

quantum asymptotic treatment proposed by Belyaev (2013) within the Born-Oppenheimer approach.

The present investigation of inelastic processes of excitation, de-excitation, mutual neutralization and ion pair formation includes 12 scattering channels: 11 channels asymptotically correspond to covalent molecular states $\text{Zn}(3d^{10}4s\,nl\,^1,^3L) + \text{H}(1s\,^2S)$ and one to ionic molecular state $\text{Zn}^+(3d^{10}4s\,^2S) + \text{H}^-(1s^2\,^1S)$. The ionic molecular state forms $^2\Sigma^+$ molecular symmetry, and only those covalent states that have $^2\Sigma^+$ symmetry are included into consideration. All the states are collected in Table 2 together with their asymptotic energies and statistical probabilities for population of $^2\Sigma^+$ molecular states. For the considered molecular states the diabatic Hamiltonian matrix is constructed, diagonalization of this matrix gives the adiabatic molecular potentials.

Non-adiabatic nuclear dynamics is investigated using the analytical multichannel formulas (see, e.g. Belyaev et al. 2014; Yakovleva et al. 2016) based on the Landau-Zener

Table 2. ZnH ($k^2\Sigma^+$) molecular states (in the LS representation), the corresponding scattering channels, their asymptotic energies with respect to the ground-state from NIST (Kramida et al. 2021), and the statistical probabilities p_k^{stat} for population of the molecular states $^2\Sigma^+$.

k	Scattering channels	Asymptotic energies (eV)	p_k^{stat}
1	$\text{Zn}(3d^{10}4s^2\ ^1S) + \text{H}(1s\ ^2S)$	0.000000	1
2	$\text{Zn}(3d^{10}4s4p\ ^3P^\circ) + \text{H}(1s\ ^2S)$	4.077881	$1/9$
3	$\text{Zn}(3d^{10}4s4p\ ^1P^\circ) + \text{H}(1s\ ^2S)$	5.795691	$1/3$
4	$\text{Zn}(3d^{10}4s5s\ ^3S) + \text{H}(1s\ ^2S)$	6.654509	$1/3$
5	$\text{Zn}(3d^{10}4s5s\ ^1S) + \text{H}(1s\ ^2S)$	6.916981	1
6	$\text{Zn}(3d^{10}4s5p\ ^3P^\circ) + \text{H}(1s\ ^2S)$	7.604056	$1/9$
7	$\text{Zn}(3d^{10}4s4d\ ^1D) + \text{H}(1s\ ^2S)$	7.743871	$1/5$
8	$\text{Zn}(3d^{10}4s4d\ ^3D) + \text{H}(1s\ ^2S)$	7.783354	$1/15$
9	$\text{Zn}(3d^{10}4s5p\ ^1P^\circ) + \text{H}(1s\ ^2S)$	7.799899	$1/3$
10	$\text{Zn}(3d^{10}4s6s\ ^3S) + \text{H}(1s\ ^2S)$	8.112569	$1/3$
11	$\text{Zn}(3d^{10}4s6s\ ^1S) + \text{H}(1s\ ^2S)$	8.187627	1
12	$\text{Zn}^+(3d^{10}4s\ ^2S) + \text{H}^-(1s^2\ ^1S)$	8.640197	1

model for individual non-adiabatic transitions. Knowing the state-to-state transition probabilities, the inelastic processes cross sections and rate coefficients are calculated by the standard formulas.

The detailed formulae for calculations of the cross sections and the rate coefficients are written for example in Belyaev et al. (2014); Yakovleva et al. (2016). The rate coefficients have the units of cm^3s^{-1} and the physical meaning of the product of velocities and cross sections averaged over the Maxwellian distribution. Being a result of multiplication of the rate coefficient defined above by the concentration of collided partners, the collision rates are entered in the SE equations and determine populations of atomic states.

The derived rate coefficients are presented in Table 3, and the graphical representation of the calculated rate coefficients at the temperature $T = 6000\text{ K}$ is given in Fig. 4. Rate coefficients are plotted with color according to their values, the study does not treat elastic processes and they are plotted by white. Fig. 4 shows that the highest values of the rate coefficients correspond to several partial mutual neutralization processes to the final scattering channels $\text{Zn}(3d^{10}4s5s\ ^1S)$, $\text{Zn}(3d^{10}4s5p\ ^3P^\circ)$, $\text{Zn}(3d^{10}4s4d\ ^{1,3}D)$, $\text{Zn}(3d^{10}4s5p\ ^1P^\circ) + \text{H}(1s\ ^2S_{1/2})$ (transitions $18 \rightarrow 5-9$).

It is worth emphasizing that nowadays it is well recognized that the so-called classical Drawin formula (Drawin 1968, 1969; Steenbock & Holweger 1984) widely used in the past for estimating H-collision rate coefficients does not have a correct physical background and therefore does not yield reliable rate coefficients. Moreover, it has been shown in Barklem et al. (2011) that for optically allowed transitions

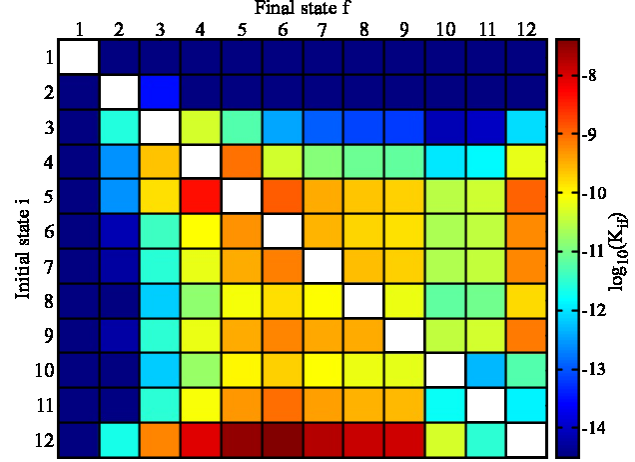


Figure 4. The graphical representation of the rate coefficients for excitation, de-excitation, neutralization and ion-pair formation processes in $\text{Zn} + \text{H}$ and $\text{Zn}^+ + \text{H}^-$ collisions at temperature $T = 6000\text{ K}$. Initial and final state labels are presented in Table 2.

the Drawin formula can overestimate rate coefficients up to a factor of several orders of magnitude, while it can underestimate optically forbidden transitions by several orders of magnitude. This means that no "correction factor" can be applied to rate coefficients obtained by the Drawin formula in order to get correct absolute values of rate coefficients, as well as to get correct ratios of rate coefficients, which are very important for non-LTE stellar atmosphere modeling. The proper way is to calculate a corresponding rate coefficient for each inelastic transition, as it is done in the present paper.

2.2 Programs and model atmospheres

The coupled radiative transfer and statistical equilibrium equations were solved with a revised version of the DETAIL code (Butler & Giddings 1985). The opacity package was updated for applications of the DETAIL code to FGK and BA stars. The updates were presented by Mashonkina et al. (2011) and Przybilla et al. (2011), respectively.

For synthetic spectra calculations, we use the SYNTHV_NLTE code (Tsymbal et al. 2019) mounted to the IDL BINMAG code by Kochukhov (2018)³. This technique allows to obtain the best fit to the observed line profiles with the NLTE effects taken into account via pre-calculated departure coefficients for a given model atmosphere.

For late type stars, we used classical plane-parallel model atmospheres from the MARCS model grid (Gustafsson et al. 2008), which were interpolated for given T_{eff} , $\log g$, and $[\text{Fe}/\text{H}]$. For BA stars, the model atmospheres were calculated under the LTE assumption with the code LLMODELS (Shulyak et al. 2004).

The lines of Zn I and Zn II selected for model atom testing and abundance determination are listed in Table 4. For the majority of the selected lines, their oscillator strengths originate from laboratory measurements. An exception is Zn I 6362 Å line, with calculated $\log gf =$

³ <https://www.astro.uu.se/~oleg/binmag.html>

Table 3. Rate coefficients (in $\text{cm}^3 \text{s}^{-1}$) for excitation, de-excitation, neutralization and ion-pair formation processes in $\text{Zn} + \text{H}$ and $\text{Zn}^+ + \text{H}^-$ collisions at different temperatures.

init. ↓ fin. →	4s ^1S	4p $^3\text{P}^\circ$	4p $^1\text{P}^\circ$	5s ^3S	5s ^1S	5p $^3\text{P}^\circ$	4d ^1D	4d ^3D	5p $^1\text{P}^\circ$	6s ^3S	6s ^1S	$\text{Zn}^+ + \text{H}^-$
T = 1000 K												
4s ^1S	–	7.48E-38	7.82E-49	6.58E-54	4.36E-56	7.46E-59	9.85E-60	5.00E-60	3.81E-60	6.95E-62	3.35E-62	2.12E-62
4p $^3\text{P}^\circ$	2.96E-18	–	1.29E-21	2.94E-27	1.25E-29	1.25E-32	1.53E-33	7.61E-34	5.70E-34	1.67E-35	9.57E-36	1.89E-36
4p $^1\text{P}^\circ$	4.22E-20	1.76E-12	–	8.04E-15	2.12E-17	1.16E-20	1.32E-21	6.40E-22	4.74E-22	1.62E-23	1.06E-23	1.13E-24
5s ^3S	7.55E-21	8.54E-14	1.71E-10	–	2.89E-11	6.40E-15	6.60E-16	3.12E-16	2.28E-16	8.16E-18	5.80E-18	4.13E-19
5s ^1S	3.16E-21	2.29E-14	2.85E-11	1.82E-09	–	2.50E-12	2.31E-13	1.06E-13	7.61E-14	2.69E-15	2.00E-15	1.08E-16
5p $^3\text{P}^\circ$	1.74E-21	7.39E-15	5.03E-12	1.30E-10	8.06E-10	–	1.18E-10	4.81E-11	3.28E-11	1.12E-12	9.10E-13	4.91E-14
4d ^1D	2.10E-21	8.25E-15	5.21E-12	1.23E-10	6.79E-10	1.07E-09	–	2.88E-10	1.72E-10	4.24E-12	3.38E-12	2.00E-13
4d ^3D	5.62E-22	2.16E-15	1.33E-12	3.05E-11	1.64E-10	2.31E-10	1.52E-10	–	1.04E-10	1.63E-12	1.28E-12	7.74E-14
5p $^1\text{P}^\circ$	2.59E-21	9.80E-15	5.97E-12	1.35E-10	7.15E-10	9.55E-10	5.50E-10	6.32E-10	–	8.89E-12	6.99E-12	4.21E-13
6s ^3S	1.78E-21	1.08E-14	7.71E-12	1.82E-10	9.51E-10	1.23E-09	5.10E-10	3.71E-10	3.35E-10	–	1.22E-12	6.08E-14
6s ^1S	6.16E-21	4.44E-14	3.61E-11	9.28E-10	5.06E-09	7.15E-09	2.92E-09	2.10E-09	1.89E-09	8.74E-12	–	2.77E-14
$\text{Zn}^+ + \text{H}^-$	7.42E-19	1.67E-12	7.34E-10	1.26E-08	5.24E-08	7.37E-08	3.29E-08	2.41E-08	2.17E-08	8.32E-11	5.30E-12	–
T = 2000 K												
...												

This table is available in its entirety in a machine-readable form in the online journal. A portion is shown here for guidance regarding its form and content.

0.14 (Biemont & Godefroid 1980). We note that, for the Zn I 4680, 4722 and 4810 Å lines, calculated log gf values are consistent within 0.02 dex with the measurements of Roederer & Lawler (2012). For Zn II 2062 Å, measurements of Mayo et al. (2006) and Roederer & Lawler (2012) provide consistent within 0.01 dex log gf.

For lines of Zn I , Van der Waals damping constants (γ_{vdW}) were calculated using the code of Barklem et al. (1998) and data from Anstee & O'Mara (1995) and Barklem & O'Mara (1997), while, for Zn II , we adopted a standard formula from Gray (2005) used in the SYNTHV_NLTE code by default. Radiative damping constant (γ_{Rad}) for the resonance lines of Zn I and Zn II were calculated from their oscillator strengths, while classical damping constants were adopted for the subordinate lines. Stark damping constants (γ_{Stark}) for Zn I lines were calculated with an approximate formula of Cowley (1971). In cool stars, Stark effect is negligible. In hot stars, Stark effect is larger, but Zn I lines in the visible range are weak. For the lines of Zn II , γ_{Stark} were taken from Bergeson & Lawler (1993). The adopted damping constants are presented in Table 4.

3 STATISTICAL EQUILIBRIUM OF Zn I-II

The ionisation threshold of neutral zinc is 9.39 eV and, in atmospheres of GK-spectral type stars, number densities of neutral and ionised zinc take values of nearly the same order of magnitude. In atmospheres of BAF-type stars, Zn II dominates. Fig. 5 shows non-LTE and LTE number densities of Zn I and Zn II in model atmospheres with different stellar parameters, which represent Sun, very metal-poor (VMP) star HD 140283, and Sirius.

The deviations from LTE are usually characterised with departure coefficients $b_i = n_{i,\text{NLTE}}/n_{i,\text{LTE}}$, where $n_{i,\text{NLTE}}$

and $n_{i,\text{LTE}}$ are non-LTE and LTE populations of i atomic level. Spectral line profiles are affected by non-LTE effects via the changes in the line opacity, which depends mainly on b_i , and the line source function, which mainly depends on the ratio of the departure coefficient of the upper and lower level (b_j/b_i). The departure coefficients for selected atomic levels of Zn I and Zn II in model atmospheres of the Sun, VMP star HD 140283, and Sirius are shown in Fig. 6. The investigated lines mostly form in layers with optical depth at $\lambda = 5000$ Å, $\log \tau_{5000} > -2.7$.

In deep atmospheric layers with $\log \tau_{5000} > 0.5$, collisions dominate, the departures from LTE are missing and the atomic levels keep their LTE populations. Non-LTE effects become more prominent towards higher atmospheric layers. When studying model atmospheres with different stellar parameters, generally, the non-LTE effects increase with increasing effective temperature and decreasing surface gravity and metallicity.

In solar atmosphere, Zn I slightly prevails upon Zn II in atmospheric layers with $\log \tau_{5000} < -0.5$, while, in deeper layers, the opposite situation arises (Fig. 5). This results in a minor depopulation of the ground state of Zn I at $\log \tau_{5000} \simeq -0.5$. Although the model atmosphere of the VMP star has close to solar T_{eff} , the ground state of Zn I is strongly depopulated in HD 140283 (Fig. 6). This happens due to smaller electron number density, stronger ionisation degree, and, thus, stronger overionisation of Zn I .

In FGK stars, the deviations from LTE for Zn I are mainly driven by bound-free transitions in metal-poor stars, while, in stars with close to solar $[\text{Fe}/\text{H}]$, bound-bound transitions are also important. For Zn I 4680, 4722, 4810 Å lines non-LTE may lead to either stronger or weaker lines depending on stellar parameters. In solar atmosphere, the line source function is smaller than the Planck function, which results in strengthened lines and negative abundance cor-

Table 4. The list of lines

Ion	λ , Å	transition	E_{exc} , eV	log gf	ref.	$\log\gamma_{\text{Rad}}$	$\log\gamma_{\text{Stark}}$	$\log\gamma_{\text{VdW}}$
Zn I	2138.573	4s ¹ S – 4p ¹ P ^o	0	0.16	A75	8.85	–5.47	–7.64
Zn I	3075.895	4s ¹ S – 4p ³ P ^o	0	–3.85	R12	4.58	–5.82	–7.86
Zn I	3302.583	4p ³ P ^o – 4d ³ D	4.03	–0.02	R12	8.31	–4.78	–7.25
Zn I	4680.136	4p ³ P ^o – 5s ³ S	4.01	–0.85	R12	8.01	–5.24	–7.30
Zn I	4722.153	4p ³ P ^o – 5s ³ S	4.03	–0.37	R12	8.00	–5.24	–7.30
Zn I	4810.528	4p ³ P ^o – 5s ³ S	4.08	–0.15	R12	7.98	–5.24	–7.30
Zn I	6362.338	4p ¹ P ^o – 4d ¹ D	5.80	0.14	BG80	7.74	–4.80	–7.30
Zn II	2025.484	4s ² S – 4p ² P ^o	0	–0.03	M06	8.61	–6.67	–7.90
Zn II	2062.001	4s ² S – 4p ² P ^o	0	–0.30	M06	8.59	–6.72	–7.90

A75 = Abjean (1975), R12 = Roederer & Lawler (2012), BG80 = Biemont & Godefroid (1980), M06 = Mayo et al. (2006)

rections. The low excitation levels 4p³P^o and 4p¹P^o are less depopulated compared to the ground state due to the radiative pumping transitions from the ground state. In stars with higher T_{eff} and/or lower [Fe/H], these lines are weak and, in contrast, become even weaker in non-LTE. In cool metal-poor stars, strong underpopulation of the ground state always results in weakened Zn I lines and positive non-LTE abundance corrections.

The levels of Zn II are overpopulated due to depopulation of Zn I levels. While in solar atmosphere this effect is small, it increases with decreasing metallicity and becomes prominent in metal-poor stars (see middle panels of Fig. 6 and also Fig. 5). An overpopulation of the ground state results in the line opacity increase and tends to strengthen resonance lines of Zn II. However, the 4p²P^o level is more overpopulated compared to the ground state of Zn II. This results in an increase in the line source function and tends to weaken resonance lines of Zn II. Which effect prevails depends on stellar parameters and the line strength. For the resonance lines of Zn II, non-LTE may lead to either positive or small in absolute value negative abundance corrections.

4 TESTING NON-LTE METHOD WITH THE REFERENCE STARS

We test our non-LTE abundance determination method with the Sun and three metal-poor stars with well-determined atmospheric parameters (Table 5).

4.1 Solar zinc abundance

Solar abundance was determined using the spectrum of the Sun as a star (Kurucz et al. 1984). The classical 1D model atmosphere with effective temperature $T_{\text{eff}} = 5780$ K, surface gravity $\log g = 4.44$, and microturbulent velocity $\xi_t = 0.9 \text{ km s}^{-1}$ was taken from the MARCS webpage⁴.

Our solar zinc abundance relies on three lines of Zn I, namely, Zn I 4722, 4810, and 6362 Å. We found an average $\log A_{\odot}^5 = -7.40 \pm 0.04$ and -7.45 ± 0.02 in LTE and

non-LTE, respectively. The abundance error is calculated as the dispersion in the single line measurements around the mean $\sigma = \sqrt{\Sigma(\log A - \log A_i)^2 / (N - 1)}$, where N is a total number of lines. For the Sun, non-LTE leads to lower zinc abundance and better agreement between abundances from different lines. Our non-LTE abundance is close to the meteoritic one $\log A_{\odot} = -7.43$ (Lodders 2021).

We compare line-by-line solar LTE abundances and non-LTE abundance corrections with results of Takeda et al. (2005). When using the same log gf values as adopted by T05, for Zn I 4722, 4810, and 6362 Å, we found $\log A_{\text{LTE}} = -7.40$, -7.40 , and -7.45 , respectively, while T05 found -7.43 , -7.50 , and -7.51 for the same lines. For Zn I 4722 and 4810 Å lines, a difference in the adopted in this study $\xi_t = 0.9 \text{ km s}^{-1}$ and 1.0 km s^{-1} in T05 translates in abundance shift of 0.04 dex and partially explains the discrepancy between the two studies. The remaining minor discrepancy can be caused by using different solar observed spectra, continuum placement and line fitting procedure. As for the non-LTE abundance correction, the agreement between the two studies is good, given that the departures from LTE are small in the solar atmosphere and different atomic data were used in the non-LTE calculations. For Zn I 4722, 4810, and 6362 Å, we found $\Delta_{\text{NLTE}} = -0.06$, -0.08 , and -0.02 , and T05 gives -0.05 , -0.05 , and 0.0 , respectively.

4.2 Zn I and Zn II lines in VMP stars

For our analysis, we selected three VMP stars with well determined stellar parameters. Their effective temperatures are based on multiple photometric determinations and surface gravities – on accurate distances. These VMP stars are turn-off star HD 84937 with $T_{\text{eff}}/\log g/[\text{Fe}/\text{H}]/\xi_t = 6350/4.09/-2.18/1.7$, subgiant HD 140283 (5780/3.70/-2.43/1.3), and giant HD 122563 (4600/1.40/-2.55/1.6). They served as the reference stars in a number of non-LTE studies (for example, Mashonkina et al. 2011, 2019; Bergemann 2011; Bergemann et al. 2017; Sitnova et al. 2016).

We adopted high resolution and high signal to noise ratio spectra in the visible range from the ESO UVESPOP survey (Bagnulo et al. 2003) and UV spectra derived at Space Telescope Imaging Spectrograph (STIS HST) from the StarCAT catalogue of Thomas Ayres⁶.

⁴ <https://marcs.astro.uu.se/>

⁵ Here $\log A(X) = \log(N_X/N_{\text{tot}})$, where N_{tot} is a total number density; X I–X II means difference in abundance derived from lines of X I and X II, $\log A(X \text{ I}) - \log A(X \text{ II})$. The abundances can be transformed to the scale relatively to the number of H atoms: $\log \varepsilon = \log A + 12.04$

⁶ <https://casa.colorado.edu/~ayres/StarCAT>

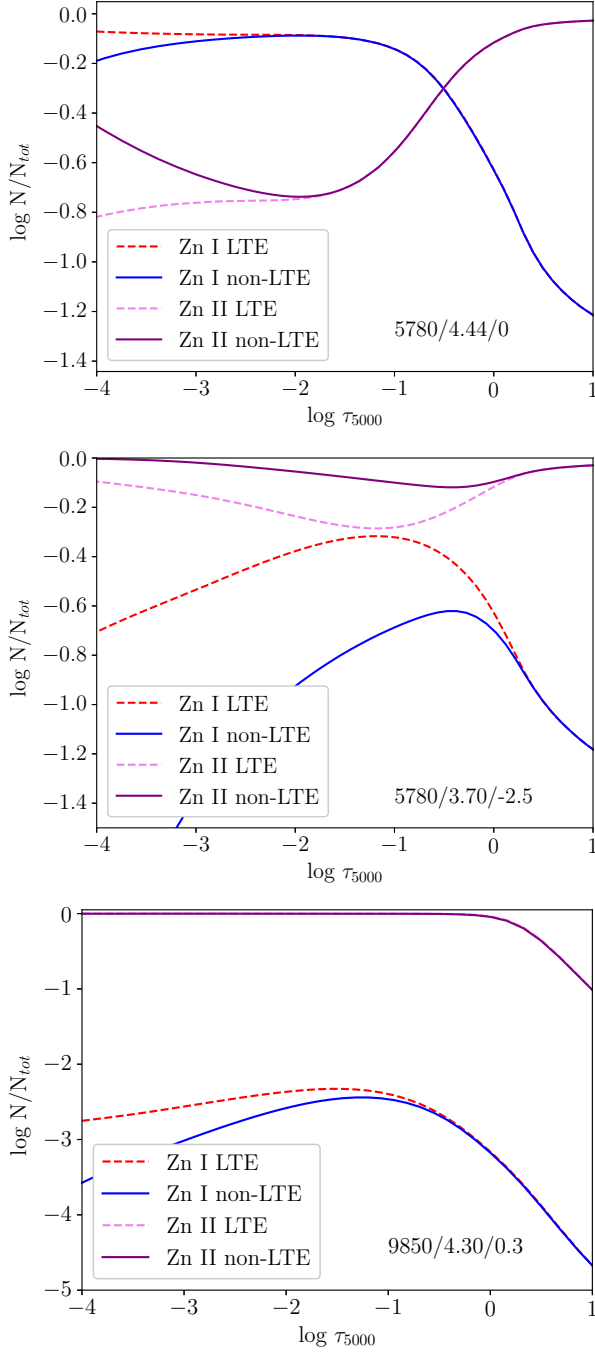


Figure 5. Non-LTE and LTE number densities of Zn I and Zn II in model atmosphere of Sun (top panel), VMP star HD 140283 (middle panel), and Sirius (bottom panel). For each model, $T_{\text{eff}}/\log g/[\text{Fe}/\text{H}]$ are indicated.

For test calculations, we determined abundances from different lines of Zn I (2138, 3075, 3302, 4810 Å) and Zn II (2025, 2062 Å) in HD 84937 and HD 140283 using different line formation scenarios:

- LTE;
- Non-LTE with electron collision rates calculated with approximate formulae as described in Sect. 2.1 and neglecting inelastic collisions with hydrogen atoms;
- Non-LTE with electron collision rates calculated with

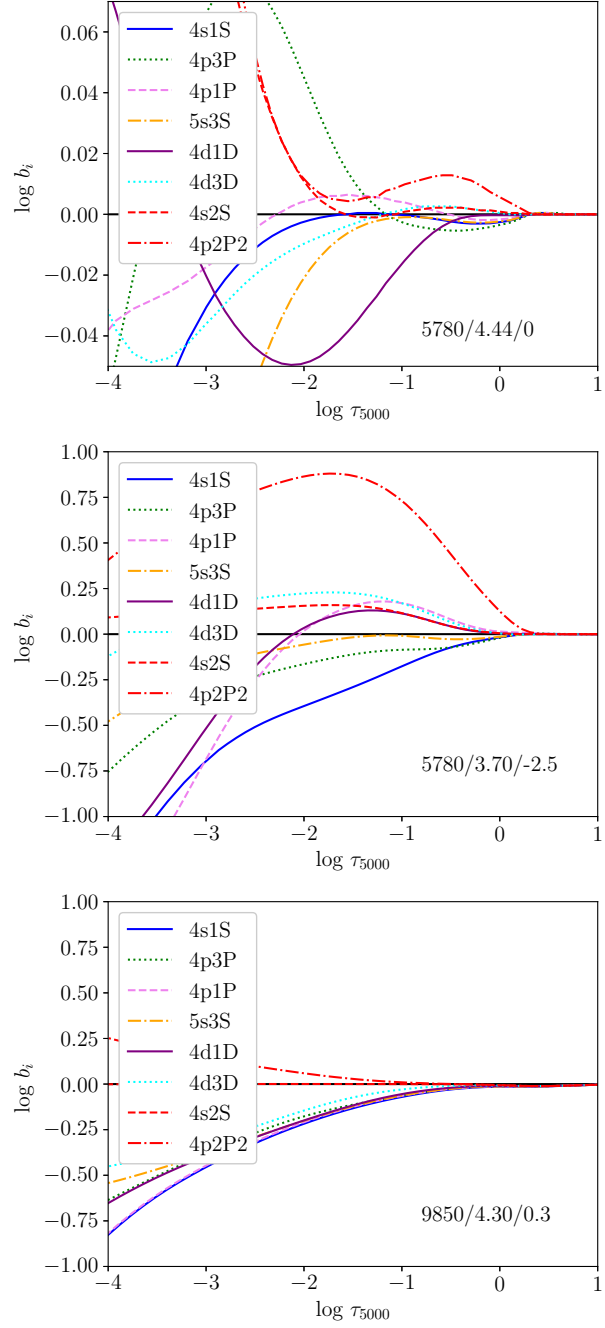


Figure 6. Departure coefficients for selected atomic levels of Zn I and Zn II in model atmosphere of Sun (top panel), VMP star HD 140283 (middle panel), and Sirius (bottom panel). For each model, $T_{\text{eff}}/\log g/[\text{Fe}/\text{H}]$ are indicated.

approximate formulae and quantum-mechanical rate coefficients for hydrogenic collisions;

- Non-LTE with accurate quantum-mechanical data for electronic and hydrogenic collisions.

Fig. 7 shows the abundances from individual lines in HD 84937 and HD 140283 derived in different line formation scenarios. In HD140283, the LTE abundance difference between any lines does not exceed 0.3 dex. LTE abundances from the subordinate lines of Zn I agree well, while the resonance line Zn I 2138 Å and the forbidden Zn I 3075 Å line

provides 0.15 dex lower and higher LTE abundance, respectively, compared to the other Zn I lines. The observed spectrum of HD 84937 does not cover the forbidden Zn I 3075 Å line, and LTE abundances between different zinc lines agree within 0.07 dex.

In non-LTE, when neglecting inelastic collisions with H atoms and using approximate electron collision rates, the departures from LTE are huge, and the non-LTE abundance correction for the resonance Zn I 2138 Å line $\Delta_{\text{NLTE}} = 0.53$ and 0.61 dex in HD 84937 and HD 140283, respectively. For the subordinate Zn I 3302 and 4810 Å lines, the corrections are smaller: 0.35 and 0.30 dex in HD 84937 and 0.37 and 0.32 dex in HD 140283.

In the investigated stars, Zn II is the majority species, and non-LTE abundance corrections for the Zn II resonance lines do not exceed 0.08 dex in absolute value in any non-LTE line formation scenario. The Zn II 2025 and 2062 Å resonance lines belong to the same multiplet, however, in HD 140283 and HD 84937, Zn II 2025 Å provides 0.1 dex higher abundance compared to the Zn II 2062 Å line, either in LTE or non-LTE. The abundance from Zn II 2025 Å can be uncertain due to blending with Fe I, Ni I, Cu II, and Cr II lines. When fitting the line profile, we varied abundances of the above elements, however, the continuum placement can be unreliable due to overlapping wings of the lines. We prefer to keep the abundance from this line as a sanity check due to the small number of zinc lines.

Including quantum-mechanical rate coefficients for inelastic collisions with H atoms decreases the departures from LTE, which results in a decrease of 0.2 dex in Δ_{NLTE} for all lines Zn I of in the two stars.

When using accurate electronic collision rates based on R-matrix calculations of Zatsarinny & Bartschat (2005), the non-LTE effects for the Zn I resonance line decreases even more, and $\Delta_{\text{NLTE}}(2138) = 0.19$ and 0.14 dex in HD 140283 and HD 84937, respectively. For the subordinate lines Zn I 3302 and 4810 Å, the changes are minor.

The latter non-LTE line formation scenario is our final one, and, for this case, the derived non-LTE abundances from different lines are presented in Table 5. In this scenario, non-LTE abundances from Zn I 2138, 3302, and 4810 Å are found to be consistent within 0.13 dex and 0.16 dex in HD 84937 and HD 140283, respectively. Either in LTE or in non-LTE, the abundance from the forbidden Zn I 3075 Å line in HD 140283 is higher compared to the other lines.

For HD 140283, we estimated an impact of uncertainties in T_{eff} , $\log g$, and ξ_t on abundances from different lines (Table 5). We adopted $\Delta T_{\text{eff}} = 50$ K (Karovicova et al. 2018), $\Delta \log g = 0.05$ dex, and $\Delta \xi_t = 0.2$ km s⁻¹ (Mashonkina et al. 2019). The above changes lead to abundance shifts of less than 0.08 dex in absolute value and cannot cancel the discrepancy between the Zn I 3075 Å line and other lines.

For HD 122563, we determined zinc abundance from the forbidden Zn I 3075 Å line and Zn I 4722 and 4810 Å lines in LTE and non-LTE, using the latter scenario. The UV spectrum of this star does not cover Zn II lines. The subordinate lines give very similar non-LTE abundances $\log A = -9.90$ and -9.91 , while lower $\log A = -10.08$ was found from the forbidden line. This behaviour is different compared to the HD 140283. We do not recommend to adopt the forbidden

Zn I 3075 Å line for zinc abundance determination neither in non-LTE, nor in LTE.

As for the Zn I – Zn II ionisation balance in HD 84937 and HD 140283, for each star, the average abundances from the two ionization stages agree within 0.08 dex either in LTE or non-LTE. For both stars, non-LTE leads to 0.17 dex higher abundance for Zn I, while, for Zn II, the non-LTE abundance is 0.06 dex and 0.03 dex higher in HD 84937 and HD 140283, respectively. Here, we excluded the Zn I 3075 Å line, when calculating the average abundance from Zn I. We found this line is an unreliable abundance indicator and we do not recommend to apply it in abundance analysis either in LTE or non-LTE.

We calculated the non-LTE abundance correction for the Zn I 2138 Å line detected by Ezzeddine et al. (2019) in the UV spectrum of hyper metal-poor star HE1327-2326. LTE zinc abundance determination together with non-LTE iron abundances results in $[\text{Zn}/\text{Fe}] = 0.80$ (Ezzeddine et al. 2019). The extremely low metallicity $[\text{Fe}/\text{H}] = -5.2$ together with high enough $T_{\text{eff}} = 6180$ K and low $\log g = 3.7$ (Frebel et al. 2005) results in dramatic departures from LTE, and $\Delta_{\text{NLTE}} = 1.03$ dex for Zn I 2138 Å line.

5 BAF TYPE STARS

We determine zinc abundance in a sample of BAF-spectral type stars with well-determined stellar parameters. For these stars, the non-LTE abundance determination was performed for a number of chemical elements, see Mashonkina et al. (2020, hereafter MR20) for details. For the summary of stellar parameter determination and description of high quality observed spectra adopted for abundance determination of the BAF stars we refer the reader to MR20. We also determined zinc abundance in Procyon, which is missing in MR20. For Procyon, we adopted stellar parameters from Ryabchikova et al. (2016), and we refer a reader to this paper for details on atmospheric parameter determination and the description of the observed spectra.

For the BAF sample stars, we determine Zn abundance from the 4680, 4722, 4810 Å lines. From one to three lines were adopted depending on their strength in the observed spectra. The derived LTE and non-LTE abundances are presented in Table 6.

The two coolest stars, HD 32115 and Procyon, are deficient in Zn in both LTE and non-LTE calculations, like the close-to-solar metallicity G dwarfs studied in Sect. 6.

In contrast, the hotter A and late B-type stars are enhanced in Zn already in LTE and even more in non-LTE. The two of them, Sirius and HD 72660, are known as metallicity (Am) stars and reveal a steep growth of abundances of the heavy elements beyond Fe (MR20, their Fig. 4). Their high values of $[\text{Zn}/\text{H}] \simeq 1$ lie well in their element abundance patterns.

The remaining three stars, HD 145788, HD 73666, and 21 Peg, reveal similar overabundances of Zn relative to Fe, with $[\text{Zn}/\text{Fe}]_{\text{non-LTE}} = 0.22$, 0.29, and 0.34, respectively. They have different metallicities because formed in the environments of different chemical composition, but very similar element abundance patterns, which resemble that for the superficially normal stars (see MR20 for a discussion and references). As found by MR20, in the superficially nor-

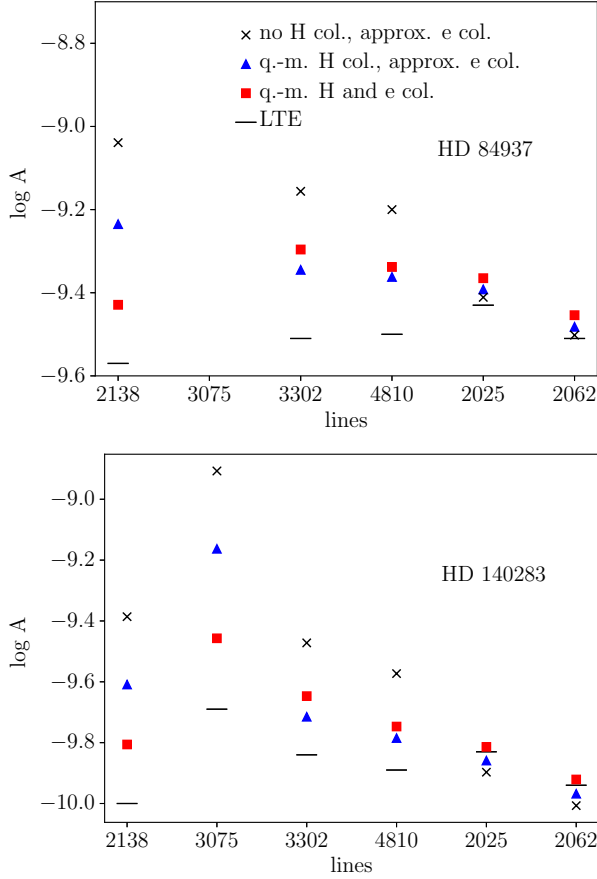


Figure 7. Zinc abundances from different lines of Zn I (2138, 3075, 3302, 4810 Å) and Zn II (2025, 2062 Å) in HD 84937 (top panel) and HD 140283 (bottom panel) at different line formation scenarios: LTE (dashes), non-LTE with neglecting H collisions and approximate electronic collisions (crosses), non-LTE with quantum-mechanical H collisions and approximate electronic collisions (triangles), non-LTE with quantum-mechanical data for H and e collisions (squares). See text for details.

mal stars, the non-LTE abundances of the chemical elements from carbon to iron are consistent within 0.1 dex with either solar (for the Galactic field stars) or scaled solar (for the star HD 73666 in the Praesepe open cluster) abundances, however, the heavy elements Sr, Zr, Ba, and Nd reveal supersolar abundances. For example, in our hottest and Galactic field star 21 Peg, $[\text{Sr}/\text{H}] = 0.59$, $[\text{Zr}/\text{H}] = 0.35$, $[\text{Ba}/\text{H}] = 0.98$, and $[\text{Nd}/\text{H}] = 0.48$. The obtained high abundances of Zn support the abundance trends found by MR20.

6 ZINC ABUNDANCE IN THE SAMPLE OF FGK DWARFS IN A WIDE METALLICITY RANGE

The FGK sample stars are listed in Table 7 together with their stellar atmosphere parameters taken from our previous studies (Sitnova et al. 2015; Mashonkina et al. 2019, 2003). The stars cover the $-2.5 \leq [\text{Fe}/\text{H}] \leq 0.2$ metallicity range. Sitnova et al. (2015) and Mashonkina et al. (2019) determined atmospheric parameters with a common method, which is based on photometric T_{eff} and distance-based log g

Table 5. LTE and non-LTE line-by-line zinc abundances in the reference stars

Lines:	Zn I					Zn II		
	2138	3075	3302	4722	4810	6362	2025 ^b	2062
Sun, 5780/4.44/0.0/0.9								
LTE	–	–	–	–7.37	–7.39	–7.44	–	–
NLTE	–	–	–	–7.43	–7.47	–7.46	–	–
HD 122563, 4600/1.43/–2.55/1.6								
LTE	–	–10.14	–	–10.04	–10.04	–	–	–
NLTE	–	–10.08	–	–9.90	–9.91	–	–	–
HD 84937, 6350/4.09/–2.12/1.7								
LTE	–9.57	–	–9.51	–	–9.50	–	–9.43	–9.51
NLTE	–9.43	–	–9.30	–	–9.34	–	–9.37	–9.45
HD 140283, 5780/3.70/–2.46/1.6								
LTE	–10.00	–9.69	–9.84	–	–9.89	–	–9.83	–9.94
NLTE	–9.81	–9.46	–9.65	–	–9.75	–	–9.81	–9.92
Abundance shifts caused by changes in parameters of HD 140283								
5730	–0.05	–0.05	–0.02	–	–0.02	–	0.05	0.02
3.65	0.01	–0.01	–0.01	–	–0.01	–	–0.03	–0.04
1.4	0.01	0.01	0.00	–	0.00	–	0.07	0.08

^b - Zn II 2025 Å is blended and should be considered with a caution.

Table 6. Atmospheric parameters and the average $[\text{Zn}/\text{H}]$ in BAF sample stars

Star	T_{eff}	log g	$[\text{Fe}/\text{H}]$	ξ_t	N_l	$[\text{Zn}/\text{H}]_{\text{LTE}}$	$[\text{Zn}/\text{H}]_{\text{NLTE}}$
Procyon	6590	3.95	–0.02	1.8	3	-0.15 ± 0.08	-0.13 ± 0.10
HD 32115	7250	4.20	0.09	2.3	2	-0.38 ± 0.01	-0.25 ± 0.01
HD 73666	9380	3.78	0.24	1.8	2	0.34 ± 0.01	0.53 ± 0.01
HD 72660	9700	4.09	0.67	1.8	3	0.87 ± 0.04	1.02 ± 0.04
HD 145788	9750	3.70	0.52	1.3	1	0.55	0.74
Sirius	9850	4.30	0.30	1.8	3	0.84 ± 0.02	0.99 ± 0.02
21 Peg	10400	3.55	0.05	0.5	1	0.21	0.39

(see the above papers for the details). Mashonkina et al. (2003) also determined distance-based log g, while T_{eff} was derived from fitting the Balmer line wings.

High-resolution ($\lambda/\Delta\lambda > 45\,000$) spectra with a signal-to-noise ratio $S/N > 60$ were obtained at the 3-m telescope of the Lick Observatory with the Hamilton spectrograph or taken from the UVES⁷ and ESPaDOnS⁸ archives. We also used the spectra obtained at the 2.2-m telescope of the Calar Alto Observatory with the FOCES spectrograph and provided by K. Fuhrmann.

We employed Zn I 4722, 4810, and 6362 Å lines for zinc abundance determination in FGK dwarfs. When fitting the Zn I 6362 Å line, the Ca I 6362 Å autoionisation line was taken into account and fitted by an increase in Van Der Waals damping constant. The derived differential LTE and non-LTE abundance ratios are presented in Table 7 and Fig. 8. Our zinc abundances are derived from the line-by-line differential approach with respect to the Sun.

Metal-poor stars with $-2.5 < [\text{Fe}/\text{H}] < -1.2$ show a decrease from $[\text{Zn}/\text{Fe}]_{\text{NLTE}} = 0.3$ to 0. In the $-1.2 < [\text{Fe}/\text{H}] < -0.5$ metallicity range, the thick disk stars show an increase in $[\text{Zn}/\text{Fe}]_{\text{NLTE}}$ from 0 to 0.3 dex. Our thin disk stars span $-0.7 < [\text{Fe}/\text{H}] < 0.2$ and show a decrease in $[\text{Zn}/\text{Fe}]$

⁷ http://archive.eso.org/eso/eso_archive_main.html

⁸ <http://www.cadc-ccda.hia-ihp.nrc-cnrc.gc.ca/en/search/>

from 0.2 to -0.2 . The close-to-solar metallicity stars have $[\text{Zn}/\text{Fe}] = -0.1$, on average.

A number of studies (for example, Bensby et al. 2003; Mikolaitis et al. 2017) concluded that the observed $[\text{Zn}/\text{Fe}] - [\text{Fe}/\text{H}]$ trend is similar to $[\alpha/\text{Fe}]$. However, we found that zinc and magnesium abundances do not follow each other (see Fig 8). To make sure that the zinc abundance does not behave like the α -element abundances, we plotted, for the comparison, the $[\text{Zn}/\text{Mg}]$ abundance ratios for our sample stars, using the Mg I abundances derived by Zhao et al. (2016), Mashonkina et al. (2019), and Mashonkina et al. (2003). We found subsolar $[\text{Zn}/\text{Mg}]$ in our sample stars. Moreover, $[\text{Zn}/\text{Mg}]$ trend is not flat: in stars with $-1.5 < [\text{Fe}/\text{H}] < -0.7$, an enhancement in zinc is smaller compared to magnesium enhancement, which results in a dip in $[\text{Zn}/\text{Mg}] - [\text{Fe}/\text{H}]$ trend.

We note that throughout all the investigated metallicity range, the $[\text{Zn}/\text{Fe}]$ spread in stars with close $[\text{Fe}/\text{H}]$ is larger compared to those for $[\text{Mg}/\text{Fe}]$ and $[\text{Ti}/\text{Fe}]$ in this stellar sample. For illustrative purposes, we present $[\text{Ti}/\text{Mg}] - [\text{Fe}/\text{H}]$ trend (Fig. 8) based on our earlier results for the same sample stars (Zhao et al. 2016; Mashonkina et al. 2019, 2003). For the stars from Mashonkina et al. (2003), we evaluated $[\text{Ti}/\text{H}]$ from a differential LTE abundance analysis of the $\text{Ti II } 5336 \text{ \AA}$ line in this study. $[\text{Ti}/\text{Mg}] - [\text{Fe}/\text{H}]$ trend is flat, with $[\text{Ti}/\text{Mg}] \simeq 0$ and the scatter is small throughout all metallicity range.

The derived $[\text{Zn}/\text{Fe}]$ trend can be understood as follows. At a very metal poor regime, zinc is produced by hypernova explosions (HN, Umeda & Nomoto 2003). High $[\text{Zn}/\text{Fe}]$ decreases with increasing $[\text{Fe}/\text{H}]$ and it reaches $[\text{Zn}/\text{Fe}] = 0$ at $[\text{Fe}/\text{H}] = -1.2$. This behavior argues that the number of HNe is larger at the earlier stages of the Galaxy formation. At $[\text{Fe}/\text{H}] > -1.2$, zinc is mainly produced in supernova explosions (SN, Kobayashi et al. 2006), and their yields depend on metallicity. Zinc production is more efficient in more metal rich SNe. This causes an increase in $[\text{Zn}/\text{Fe}]$ at $-1.2 < [\text{Fe}/\text{H}] < -0.8$. For $[\text{Fe}/\text{H}] > -0.8$, $[\text{Zn}/\text{Fe}]$ decreases to the solar and subsolar values due to iron production in SN Ia.

We compared the derived $[\text{Zn}/\text{Fe}]$ trend with predictions of Kobayashi et al. (2020). Their chemical evolution model reproduces a decrease in $[\text{Zn}/\text{Fe}]$ for $[\text{Fe}/\text{H}] > -0.8$. For the lower metallicities, the observed dip at $[\text{Fe}/\text{H}] \simeq -1.2$ and an uprising trend with decreasing $[\text{Fe}/\text{H}]$ are not reproduced. It is worth noting that the fraction of HNe is set in the model as a parameter and it was assumed constant. The observed trend at $[\text{Fe}/\text{H}] < -1$ potentially could be reproduced by applying the metallicity dependent HN fraction. Our observed trend can be helpful for testing and improving the Galactic chemical evolution models.

7 A GRID OF THE NON-LTE ABUNDANCE CORRECTIONS

We calculated the non-LTE abundance corrections for cool and hot stars using MARCS and LLMODELS model atmosphere grids, respectively. For cool stars, our grid contains non-LTE abundance corrections for the seven lines of Zn I and the two resonance lines of Zn II . Our stellar parameter range covers models in a wide metallicity range ($-4 \leq [\text{Fe}/\text{H}] \leq 0.5$ with a step of 0.5 dex) for dwarfs ($5000 \text{ K} \leq$

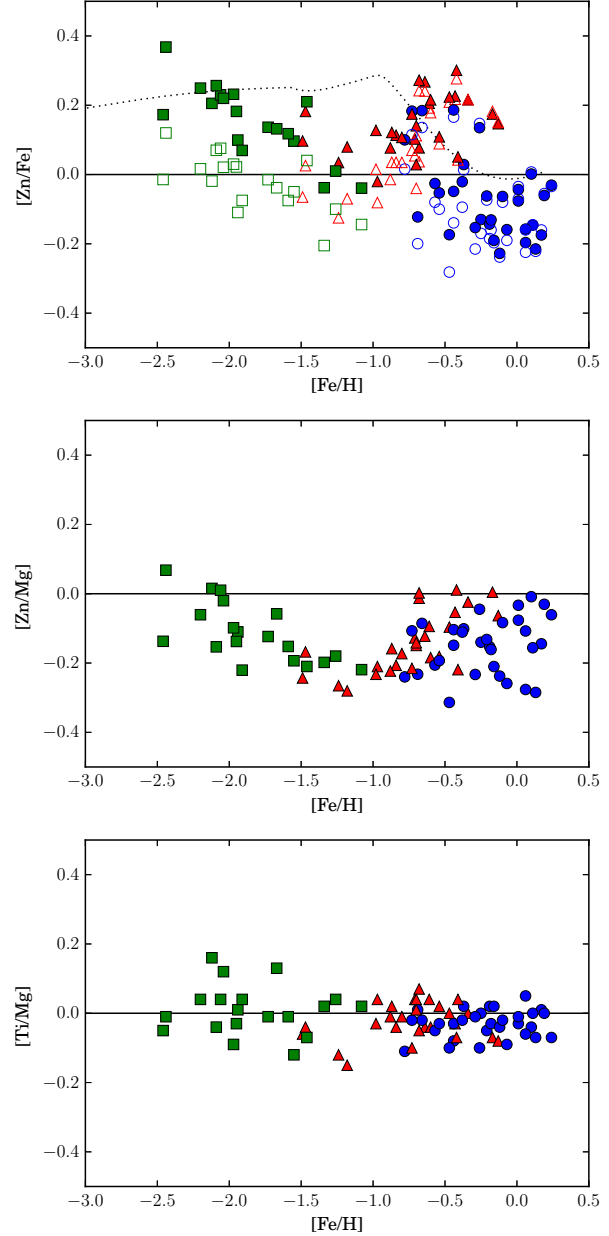


Figure 8. Galactic abundance trends for $[\text{Zn}/\text{Fe}]$ (top panel), $[\text{Zn}/\text{Mg}]$ (middle panel), and $[\text{Ti}/\text{Mg}]$ (bottom panel, for comparison). Halo, thick, and thin disk stars are shown with squares, triangles, and circles, respectively. Non-LTE and LTE abundance ratios are shown with filled and open symbols, respectively. Dotted line shows the Galactic trend predicted by Kobayashi et al. (2020).

$T_{\text{eff}} \leq 6500 \text{ K}$, $3.0 \leq \log g \leq 5.0$, $\xi_t = 1 \text{ km s}^{-1}$), subgiants ($5000 \text{ K} \leq T_{\text{eff}} \leq 5500 \text{ K}$, $2.0 \leq \log g \leq 2.5$, $\xi_t = 2 \text{ km s}^{-1}$), and giants ($4000 \text{ K} \leq T_{\text{eff}} \leq 5000 \text{ K}$, $0.5 \leq \log g \leq 2.5$, $\xi_t = 2 \text{ km s}^{-1}$). In the calculations of the non-LTE corrections, we adopted $[\text{Zn}/\text{Fe}] = 0$. To estimate an impact of the adopted $[\text{Zn}/\text{Fe}]$ on the non-LTE corrections, we performed non-LTE calculations for model atmosphere with $T_{\text{eff}}/\log g/[\text{Fe}/\text{H}] = 5500/4.0/-2$ with $[\text{Zn}/\text{Fe}] = 0.2$. In this case, we found $\Delta_{\text{NLTE}}(4810) = 0.095$, which is similar to our correction $\Delta_{\text{NLTE}}(4810) = 0.099$ found with $[\text{Zn}/\text{Fe}] = 0$.

Table 7. Stellar atmosphere parameters and zinc abundance ratios in the sample of dwarfs

HD, BD	T_{eff} , K	$\log g$	[Fe/H]	ξ_t km s ⁻¹	pop. type	[Zn/H] _{LTE}	[Zn/H] _{NLTE}	N ₁
Atmospheric parameters from Mashonkina et al. (2019):								
3795	5475	3.85	-0.61	1.0	Thick disk	-0.42 ± 0.05	-0.40 ± 0.04	3
10519	5740	4.01	-0.64	1.1	Thick disk	-0.40 ± 0.08	-0.37 ± 0.04	3
18757	5650	4.30	-0.34	1.0	Thick disk	-0.12 ± 0.06	-0.12 ± 0.06	3
32923	5710	4.03	-0.26	1.2	Thin disk	-0.11 ± 0.03	-0.12 ± 0.04	3
40397	5550	4.39	-0.17	1.0	Thick disk	0.01 ± 0.05	0.00 ± 0.06	3
55575	5960	4.29	-0.37	1.2	Thin disk	-0.36 ± 0.01	-0.34 ± 0.02	3
64606	5280	4.63	-0.68	1.0	Thick disk	-0.64 ± 0.07	-0.60 ± 0.04	3
65583	5315	4.50	-0.68	0.8	Thick disk	-0.44 ± 0.13	-0.41 ± 0.10	3
68017	5615	4.41	-0.43	0.9	Thick disk	-0.21 ± 0.03	-0.20 ± 0.03	3
69611	5940	4.17	-0.60	1.2	Thick disk	-0.42 ± 0.05	-0.38 ± 0.02	3
102158	5800	4.24	-0.47	1.1	Thick disk	-0.26 ± 0.06	-0.25 ± 0.04	3
112758	5260	4.54	-0.44	0.7	Thin disk	-0.27 ± 0.06	-0.25 ± 0.05	3
114762	5930	4.18	-0.71	1.2	Thick disk	-0.66 ± 0.03	-0.61 ± 0.03	3
132142	5100	4.47	-0.42	0.7	Thick disk	-0.14 ± 0.09	-0.12 ± 0.08	3
135204	5420	4.44	-0.13	0.9	Thick disk	0.02 ± 0.07	0.02 ± 0.08	3
144579	5250	4.49	-0.66	0.8	Thin disk	-0.52 ± 0.04	-0.48 ± 0.03	2
184499	5745	4.07	-0.54	1.2	Thick disk	-0.45 ± 0.09	-0.43 ± 0.06	3
201891	5900	4.29	-0.97	1.2	Thick disk	-1.05 ± 0.06	-0.99 ± 0.03	3
221830	5770	4.14	-0.41	1.2	Thick disk	-0.37 ± 0.05	-0.36 ± 0.04	3
222794	5600	3.90	-0.70	1.2	Thick disk	-0.59 ± 0.09	-0.56 ± 0.05	3
Atmospheric parameters from Sitnova et al. (2015):								
19373	6045	4.24	0.10	1.2	Thin disk	0.11 ± 0.06	0.10 ± 0.06	2
22484	6000	4.07	0.01	1.1	Thin disk	-0.02 ± 0.02	-0.03 ± 0.02	2
22879	5800	4.29	-0.84	1.0	Thick disk	-0.80 ± 0.02	-0.73 ± 0.03	2
30562	5900	4.08	0.17	1.3	Thin disk	0.01 ± 0.00	-0.00 ± 0.00	2
34411	5850	4.23	0.01	1.2	Thin disk	-0.06 ± 0.01	-0.07 ± 0.01	2
49933	6600	4.15	-0.47	1.7	Thin disk	-0.75 ± 0.08	-0.64 ± 0.07	2
59374	5850	4.38	-0.88	1.2	Thick disk	-0.89 ± 0.04	-0.80 ± 0.02	2
59984	5930	4.02	-0.69	1.4	Thin disk	-0.89 ± 0.03	-0.81 ± 0.03	2
64090	5400	4.70	-1.73	0.7	Halo	-1.74 ± 0.02	-1.59 ± 0.00	2
69897	6240	4.24	-0.25	1.4	Thin disk	-0.42 ± 0.01	-0.38 ± 0.01	2
84937	6350	4.09	-2.12	1.7	Halo	-2.14 ± 0.04	-1.91 ± 0.06	2
94028	5970	4.33	-1.47	1.3	Thick disk	-1.44 ± 0.04	-1.29 ± 0.05	2
102870	6170	4.14	0.11	1.5	Thin disk	-0.03 ± 0.01	-0.04 ± 0.01	2
103095	5130	4.66	-1.26	0.9	Halo	-1.36 ± 0.01	-1.25 ± 0.03	2
105755	5800	4.05	-0.73	1.2	Thin disk	-0.61 ± 0.01	-0.55 ± 0.00	2
114710	6090	4.47	0.06	1.1	Thin disk	-0.10 ± 0.00	-0.10 ± 0.00	2
134169	5890	4.02	-0.78	1.2	Thin disk	-0.76 ± 0.04	-0.68 ± 0.04	2
140283	5780	3.70	-2.46	1.6	Halo	-2.47 ± 0.04	-2.29 ± 0.02	2
142091	4810	3.12	-0.07	1.2	Thin disk	-0.26 ± 0.10	-0.23 ± 0.10	1
+66 0268	5300	4.72	-2.06	0.6	Halo	-1.98 ± 0.04	-1.83 ± 0.05	2
24289	5980	3.71	-1.94	1.1	Halo	-2.05 ± 0.03	-1.84 ± 0.01	2
30743	6450	4.20	-0.44	1.8	Thin disk	-0.58 ± 0.03	-0.49 ± 0.02	2
43318	6250	3.92	-0.19	1.7	Thin disk	-0.37 ± 0.01	-0.33 ± 0.01	2
45067	5960	3.94	-0.16	1.5	Thin disk	-0.36 ± 0.12	-0.35 ± 0.12	2
45205	5790	4.08	-0.87	1.1	Thick disk	-0.83 ± 0.02	-0.75 ± 0.03	2
52711	5900	4.33	-0.21	1.2	Thin disk	-0.28 ± 0.05	-0.27 ± 0.05	2
58855	6410	4.32	-0.29	1.6	Thin disk	-0.50 ± 0.01	-0.44 ± 0.00	2
62301	5840	4.09	-0.70	1.3	Thick disk	-0.74 ± 0.00	-0.67 ± 0.00	2
74000	6225	4.13	-1.97	1.3	Halo	-1.94 ± 0.00	-1.74 ± 0.02	2
76932	5870	4.10	-0.98	1.3	Thick disk	-0.96 ± 0.01	-0.85 ± 0.00	2
82943	5970	4.37	0.19	1.2	Thin disk	0.14 ± 0.01	0.13 ± 0.01	2
89744	6280	3.97	0.13	1.7	Thin disk	-0.09 ± 0.08	-0.08 ± 0.08	2
90839	6195	4.38	-0.18	1.4	Thin disk	-0.34 ± 0.00	-0.31 ± 0.00	2
92855	6020	4.36	-0.12	1.3	Thin disk	-0.36 ± 0.06	-0.35 ± 0.06	2
99984	6190	3.72	-0.38	1.8	Thin disk	-0.47 ± 0.04	-0.40 ± 0.03	2
100563	6460	4.32	0.06	1.6	Thin disk	-0.16 ± 0.10	-0.14 ± 0.10	2
106516	6300	4.44	-0.73	1.5	Thick disk	-0.66 ± 0.00	-0.56 ± 0.01	2
108177	6100	4.22	-1.67	1.1	Halo	-1.71 ± 0.06	-1.54 ± 0.04	2
110897	5920	4.41	-0.57	1.2	Thin disk	-0.65 ± 0.01	-0.60 ± 0.02	2
115617	5490	4.40	-0.10	1.1	Thin disk	-0.18 ± 0.01	-0.16 ± 0.02	2
134088	5730	4.46	-0.80	1.1	Thick disk	-0.76 ± 0.01	-0.69 ± 0.02	2
138776	5650	4.30	0.24	1.3	Thin disk	0.21 ± 0.10	0.21 ± 0.10	2
142373	5830	3.96	-0.54	1.4	Thin disk	-0.64 ± 0.10	-0.59 ± 0.10	1
-4 3208	6390	4.08	-2.20	1.4	Halo	-2.18 ± 0.05	-1.95 ± 0.06	2
+7 4841	6130	4.15	-1.46	1.3	Halo	-1.42 ± 0.03	-1.25 ± 0.01	2
+9 0352	6150	4.25	-2.09	1.3	Halo	-2.02 ± 0.00	-1.83 ± 0.01	2
+24 1676	6210	3.90	-2.44	1.5	Halo	-2.32 ± 0.10	-2.07 ± 0.10	1
+29 2091	5860	4.67	-1.91	0.8	Halo	-1.98 ± 0.02	-1.84 ± 0.00	2
+37 1458	5500	3.70	-1.95	1.0	Halo	-1.93 ± 0.06	-1.77 ± 0.07	2
090-03	6007	3.90	-2.04	1.3	Halo	-2.02 ± 0.04	-1.82 ± 0.06	2
Atmospheric parameters from Mashonkina et al. (2003):								
29907	5500	4.64	-1.55	0.6	Halo	-1.60 ± 0.01	-1.45 ± 0.00	2
31128	5980	4.49	-1.49	1.2	Thick disk	-1.55 ± 0.01	-1.39 ± 0.02	2
59392	6010	4.02	-1.59	1.4	Halo	-1.66 ± 0.01	-1.47 ± 0.02	2
97320	6110	4.27	-1.18	1.4	Thick disk	-1.25 ± 0.00	-1.10 ± 0.02	2
193901	5780	4.46	-1.08	0.9	Halo	-1.22 ± 0.04	-1.12 ± 0.05	2
298986	6130	4.30	-1.34	1.4	Halo	-1.54 ± 0.01	-1.38 ± 0.02	2
102200	6115	4.20	-1.24	1.4	Thick disk	-1.36 ± 0.01	-1.21 ± 0.01	2
								[Ti/H] ¹
								-1.38
								-1.21
								-1.33
								-0.97
								-0.88
								-1.16
								-1.06

¹ - determined in this study

For hot stars, our grid of non-LTE corrections spans in the following range of stellar parameters: $6600 \text{ K} \leq T_{\text{eff}} \leq 11000 \text{ K}$ with a step of 200 K for $T_{\text{eff}} \leq 10000 \text{ K}$ and 250 K for higher T_{eff} s, $3.0 \leq \log g \leq 5.0$ with a step of 0.2 dex, $-0.5 \leq [\text{Fe}/\text{H}] \leq 0.5$ with a step of 0.5 dex, and $\xi_t = 2 \text{ km s}^{-1}$. The calculations were performed with $[\text{Zn}/\text{Fe}] = 0$.

Although we do not analyse Zn II lines in our sample hot stars, in the literature, there are studies based on Zn II UV lines (Sadakane et al. 1988; Smith 1994). Therefore, we provide the non-LTE corrections for these lines. In A type stars, Zn II dominates, and, for the resonance Zn II lines, non-LTE corrections are small. For example, for model atmosphere with $T_{\text{eff}} = 11000 \text{ K}$, $\log g = 3$, $[\text{Fe}/\text{H}] = 0.0$, Δ_{NLTE} (2025, 2062) = 0.06 dex, and the corrections are smaller for model atmospheres with lower T_{eff} and larger $\log g$. Thus, the results of Sadakane et al. (1988) and Smith (1994) are weakly affected by the non-LTE effects.

Fig. 9 shows the behaviour of the non-LTE abundance corrections for different spectral lines and atmospheric parameters. The correction for Zn I 4810 Å line strongly depends on the line strength (or metallicity) and it changes its sign at $[\text{Fe}/\text{H}] \simeq -1$. Neglecting non-LTE effects when studying stars in a wide metallicity range distorts the Galactic $[\text{Zn}/\text{Fe}]$ trend (see, for example, open symbols in Fig. 8, top panel).

For model atmospheres with $T_{\text{eff}} = 5500 \text{ K}$ and 6500 K , $\log g = 4$, and $[\text{Fe}/\text{H}] = 0, -1, -2, -3$, we compared the derived non-LTE corrections for Zn I 4810 and 6362 Å lines with results of T05. For solar metallicity, both studies provide similar results, and the difference in non-LTE corrections is smaller than 0.02 dex (Fig. 9). In metal-poor model atmospheres, there is no agreement between the two studies. For the Zn I 4810 Å line, our corrections are systematically 0.1 dex larger compared to those of T05. Using different methods, namely, codes, model atoms, and atomic data results in different abundance corrections for metal-poor stars.

8 CONCLUSIONS

We investigated the departures from LTE for Zn I–Zn II in a wide range of stellar parameters with a new model atom of Zn I–Zn II based on the most up-to-date data on the photoionisation cross-sections, electron-impact excitation rates for Zn I, and the Zn I + H I and Zn II + H⁺ collisions. The latter are treated with the rate coefficients, which were calculated in this study for the first time using the multi-channel quantum asymptotic treatment based on the Born-Oppenheimer approach. The non-LTE calculations for Zn I–Zn II were performed through a range of spectral types from G to late B.

Using Zn I 4722, 4810, and 6362 Å lines, we determined solar zinc abundance $\log A_{\odot} = -7.40 \pm 0.04$ and -7.45 ± 0.02 in LTE and non-LTE, respectively. For the Sun, non-LTE leads to lower zinc abundance and better agreement between abundances from different lines. Our non-LTE abundance is close to the meteoritic one $\log A = -7.43$ (Lodders 2021).

Non-LTE analysis was performed for the first time for the UV Zn I and Zn II lines in two very metal-poor reference stars, HD 84937 and HD 140283. We found consistent non-LTE abundance from the resonance Zn I 2138 Å line, the

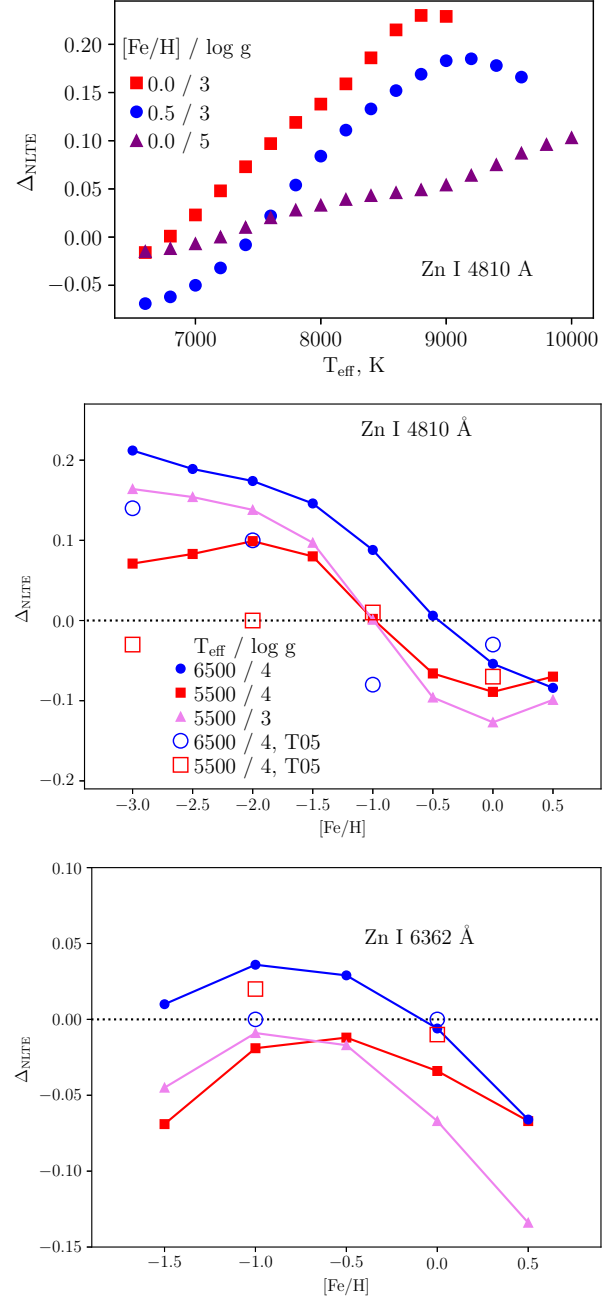


Figure 9. Non-LTE abundance corrections for the selected stellar parameters in a grid of LLMOLELS (top panel) and MARCS (middle and bottom panels) model atmospheres. The spectral lines are indicated. For comparison, we present non-LTE corrections from T05 (open symbols).

subordinate lines, and the lines of Zn II. In both stars, non-LTE leads to 0.17 dex higher average abundance from Zn I, while, for Zn II lines, non-LTE corrections are minor and do not exceed 0.06 dex.

Using the Zn I lines in the visible high-resolution spectra, we determined non-LTE abundances for a sample of 80 dwarf stars in the $-2.5 \leq [\text{Fe}/\text{H}] \leq 0.2$ metallicity range. Metal-poor stars with $-2.5 < [\text{Fe}/\text{H}] < -1.2$ show a decrease from $[\text{Zn}/\text{Fe}]_{\text{NLTE}} = 0.3$ to 0. In the $-1.2 < [\text{Fe}/\text{H}] < -0.5$ metallicity range, the thick disk stars show an in-

Table 8. Non-LTE abundance corrections and equivalent widths for zinc lines as a function of T_{eff} , $\log g$, and $[\text{Fe}/\text{H}]$ in MARCS and LL model atmosphere grids.

λ , nm	species	E_{exc} , eV	$\log gf$				
T_{eff} , K	$\log g_1$	$\log g_2$...	$\log g_8$	$\log g_9$	$\log g_{10}$	
$[\text{Fe}/\text{H}]_1$	EW ₁	EW ₂	...	EW ₈	EW ₉	EW ₁₀	
$[\text{Fe}/\text{H}]_1$	Δ_1	Δ_2	...	Δ_8	Δ_9	Δ_{10}	
...							
213.8573 nm	Zn I	$E_{\text{exc}} = 0.000$	$\log gf = 0.161$				
$T_{\text{eff}} = 5000$	0.5	1.0	...	4.0	4.5	5.0	
	0.5	-1	-1	...	-1	-1	
	0.5	-1.000	-1.000	...	-1.000	-1.000	
	0.0	-1	-1	...	-1	-1	
	0.0	-1.000	-1.000	...	-1.000	-1.000	
	-0.5	-1	-1	...	-1	-1	
	-0.5	-1.000	-1.000	...	-1.000	-1.000	
	-1.0	-1	-1	...	-1	-1	
	-1.0	-1.000	-1.000	...	-1.000	-1.000	
	-1.5	-1	-1	...	-1	-1	
	-1.5	-1.000	-1.000	...	-1.000	-1.000	
	-2.0	-1	-1	...	-1	-1	
	-2.0	-1.000	-1.000	...	-1.000	-1.000	
	-2.5	-1	-1	...	-1	-1	
	-2.5	-1.000	-1.000	...	-1.000	-1.000	
	-3.0	-1	-1	...	-1	-1	
	-3.0	-1.000	-1.000	...	-1.000	-1.000	
	-3.5	140	136	...	207	230	255
	-3.5	0.681	0.642	...	0.089	0.050	0.027
	-4.0	97	95	...	123	136	151
	-4.0	0.709	0.667	...	0.097	0.056	0.033

This table is available in its entirety in a machine-readable form in the online journal. A portion is shown here for guidance regarding its form and content. If $\text{EW} = -1$ and $\Delta_{\text{NLTE}} = -1$, this means that EW is either $< 3 \text{ m\AA}$ or $> 300 \text{ m\AA}$ in a given model atmosphere.

crease in $[\text{Zn}/\text{Fe}]_{\text{NLTE}}$ from 0 to 0.3 dex. Our thin disk stars span $-0.7 < [\text{Fe}/\text{H}] < 0.2$ and show a decrease in $[\text{Zn}/\text{Fe}]$ from 0.2 to -0.2 . The close-to-solar metallicity stars have $[\text{Zn}/\text{Fe}] = -0.1$, on average.

We compared the derived $[\text{Zn}/\text{Fe}]$ trend with predictions of Kobayashi et al. (2020). Their chemical evolution model reproduces a decrease in $[\text{Zn}/\text{Fe}]$ for $[\text{Fe}/\text{H}] > -0.5$. For the lower metallicities, the observed dip at $[\text{Fe}/\text{H}] \simeq -1.2$ and an uprising trend with decreasing $[\text{Fe}/\text{H}]$ are not reproduced by the model. The derived trend argues for zinc production in the most massive stars and metallicity dependent yields.

For the first time we perform the non-LTE abundance determination of zinc in BAF spectral type stars. For the subordinate Zn I 4680, 4722, 4810 Å lines, non-LTE leads to either negative, or positive abundance corrections depending on stellar parameters. Non-LTE abundances of zinc were derived for the first time for seven reference F to late B-type stars. HD 32115 and Procyon are deficient in zinc with $[\text{Zn}/\text{Fe}] = -0.34$ and -0.11 , respectively. This result is in line with the $[\text{Zn}/\text{Fe}]$ in close-to-solar metallicity G dwarfs.

The hotter A and late B-type stars are, in contrast, enhanced in zinc already in LTE and even more in non-LTE. The two of them, Sirius and HD 72660, are known as metallic-line stars and reveal a steep growth of abundances of the heavy elements beyond iron. Their high values of $[\text{Zn}/\text{H}] \simeq 1$ lie well in their element abundance patterns.

The remaining three stars, HD 145788, HD 73666, and 21 Peg, reveal similar $[\text{Zn}/\text{Fe}] = 0.22, 0.29$, and 0.34 , respectively. They have different metallicities because formed in the environments of different chemical composition, but

very similar element abundance patterns, which resemble that for the superficially normal stars. However, in these stars, Mashonkina et al. (2020) found supersolar abundance ratios for the heavy elements Sr, Zr, Ba, and Nd, and the obtained high abundances of Zn support the abundance trends found by MR20.

To account for deviations from LTE, we provide non-LTE abundance corrections for individual lines of zinc in a wide range of stellar parameters.

ACKNOWLEDGMENTS

We thank Klaus Bartschat for providing the data for electron impact excitation of Zn I in digital form. The authors are grateful to Klaus Fuhrmann for providing the spectra obtained with the FOCES spectrograph on the 2.2 m telescope of the Calar Alto Observatory. We also thank the referee for the notes and suggestions, which substantially helped to improve the paper. TS is grateful to Prof. Chia-ki Kobayashi for useful comments on the derived Galactic trend. TS acknowledges support from the BASIS Foundation, Project No. 20-1-3-10-1. SAY gratefully acknowledges support from the Ministry of Education (the Russian Federation), Project No. FSZN-2020-0026. AKB gratefully acknowledges support from the Basis foundation, Project No. 20-1-1-33-1. We made use of the StarCAT, NIST, SIMBAD, VALD, and R. Kurucz databases.

9 DATA AVAILABILITY

The data used in this article will be shared on request to the corresponding author.

REFERENCES

- Abjean R., 1975, *J. Quant. Spec. Radiat. Transf.*, 15, 25
- Anstee S. D., O’Mara B. J., 1995, *MNRAS*, 276, 859
- Bagnulo S., Jehin E., Ledoux C., Cabanac R., Melo C., Gilmozzi R., ESO Paranal Science Operations Team 2003, *The Messenger*, 114, 10
- Barklem P. S., Anstee S. D., O’Mara B. J., 1998, *PASA*, 15, 336
- Barklem P. S., Belyaev A. K., Guitou M., Feautrier N., Gad  a F. X., Spielfiedel A., 2011, *A&A*, 530, A94
- Barklem P. S., O’Mara B. J., 1997, *MNRAS*, 290, 102
- Belyaev A. K., 2013, *Phys. Rev. A*, 88, 052704
- Belyaev A. K., Yakovleva S. A., Barklem P. S., 2014, *A&A*, 572, A103
- Bensby T., Feltzing S., Lundstr  m I., 2003, *A&A*, 410, 527
- Bensby T., Feltzing S., Lundstr  m I., Ilyin I., 2005, *A&A*, 433, 185
- Bensby T., Feltzing S., Oey M. S., 2014, *A&A*, 562, A71
- Berg T. A. M., Ellison S. L., S  nchez-Ram  rez R., Prochaska J. X., Lopez S., D’Odorico V., Becker G., Christensen L., Cupani G., Denney K., Worseck G., 2016, *MNRAS*, 463, 3021
- Bergemann M., 2011, *MNRAS*, 413, 2184
- Bergemann M., Collet R., Amarsi A. M., Kovalev M., Ruchti G., Magic Z., 2017, *ApJ*, 847, 15
- Bergeson S. D., Lawler J. E., 1993, *ApJ*, 408, 382

- Biemont E., Godefroid M., 1980, *A&A*, 84, 361
- Butler K., Giddings J., 1985, Newsletter on the analysis of astronomical spectra, No. 9, University of London
- Cayrel R., Depagne E., Spite M., Hill V., Spite F., François P., Plez B., Beers T., Primas F., Andersen J., Barbuy B., Bonifacio P., Molaro P., Nordström B., 2004, *A&A*, 416, 1117
- Chen Y. Q., Nissen P. E., Zhao G., 2004, *A&A*, 425, 697
- Cowley C. R., 1971, *The Observatory*, 91, 139
- Drawin H.-W., 1968, *Zeitschrift für Physik*, 211, 404
- Drawin H. W., 1969, *Zeitschrift für Physik*, 225, 483
- Duffau S., Caffau E., Sbordon L., Bonifacio P., Andrievsky S., Korotin S., Babusiaux C., Salvadori S., Monaco L., François P., Skúladóttir Á., 2017, *A&A*, 604, A128
- Ezzeddine R., Frebel A., Roederer I. U., Tominaga N., Tumlinson J., Ishigaki M., Nomoto K., Placco V. M., Aoki W., 2019, *ApJ*, 876, 97
- Frebel A., Aoki W., Christlieb N., Ando H., Asplund M., Barklem P. S., Beers T. C., Eriksson K., Fechner C., Fujimoto M. Y., Honda S., Kajino T., Minezaki T., Nomoto K., Norris J. E., Ryan S. G., Takada-Hidai M., Tsangarides S., Yoshii Y., 2005, *Nature*, 434, 871
- Gray D. F., 2005, *The Observation and Analysis of Stellar Photospheres*
- Gustafsson B., Edvardsson B., Eriksson K., Jørgensen U. G., Nordlund Å., Plez B., 2008, *A&A*, 486, 951
- Karovicova I., White T. R., Nordlander T., Lind K., Casagrande L., Ireland M. J., Huber D., Creevey O., Mourard D., Schaefer G. H., Gilmore G., Chiavassa A., Wittkowski M., Jofré P., Heiter U., Thévenin F., Asplund M., 2018, *MNRAS*, 475, L81
- Kobayashi C., Karakas A. I., Lugaro M., 2020, *ApJ*, 900, 179
- Kobayashi C., Umeda H., Nomoto K., Tominaga N., Ohkubo T., 2006, *ApJ*, 653, 1145
- Kochukhov O., 2018, *BinMag: Widget for comparing stellar spectra observed with theoretical spectra*
- Kramida A., Yu. Ralchenko Reader J., and NIST ASD Team, 2021, *NIST Atomic Spectra Database (ver. 5.9)*, [Online]. Available: <https://physics.nist.gov/asd> [2021, November 9]. National Institute of Standards and Technology, Gaithersburg, MD.
- Kurucz R. L., Furenlid I., Brault J., Testerman L., 1984, *Solar flux atlas from 296 to 1300 nm*
- Liu Y. P., Gao C., Zeng J. L., Shi J. R., 2011, *A&A*, 536, A51
- Lodders K., 2021, *Space Sci. Rev.*, 217, 44
- Lodders K., Palme H., Gail H.-P., 2009, *Landolt Börnstein Mashonkina L., Gehren T., Shi J.-R., Korn A. J., Grupp F., 2011, A&A, 528, A87*
- Mashonkina L., Gehren T., Travaglio C., Borkova T., 2003, *A&A*, 397, 275
- Mashonkina L., Ryabchikova T., Alexeeva S., Sitnova T., Zatsarinny O., 2020, *MNRAS*, 499, 3706
- Mashonkina L., Sitnova T., Yakovleva S. A., Belyaev A. K., 2019, *A&A*, 631, A43
- Mashonkina L. I., Neretina M. D., Sitnova T. M., Pakhomov Y. V., 2019, *Astronomy Reports*, 63, 726
- Mayo R., Ortiz M., Campos J., 2006, *European Physical Journal D*, 37, 181
- Mikolaitis Š., de Laverny P., Recio-Blanco A., Hill V., Worley C. C., de Pascale M., 2017, *A&A*, 600, A22
- Mishenina T. V., Kovtyukh V. V., Soubiran C., Travaglio C., Busso M., 2002, *A&A*, 396, 189
- Nissen P. E., Chen Y. Q., Asplund M., Pettini M., 2004, *A&A*, 415, 993
- Primas F., Brugamyer E., Sneden C., King J. R., Beers T. C., Boesgaard A. M., Deliyannis C. P., 2000, in Noels A., Magain P., Caro D., Jehin E., Parmentier G., Thoul A. A., eds, *Liege International Astrophysical Colloquia Vol. 35 of Liege International Astrophysical Colloquia, Copper and zinc abundances in metal-poor stars*. p. 119
- Przybilla N., Nieva M.-F., Butler K., 2011, *Journal of Physics Conference Series*, 328, 012015
- Reddy B. E., Tomkin J., Lambert D. L., Allende Prieto C., 2003, *MNRAS*, 340, 304
- Roederer I. U., Barklem P. S., 2018, *ApJ*, 857, 2
- Roederer I. U., Lawler J. E., 2012, *ApJ*, 750, 76
- Roederer I. U., Placco V. M., Beers T. C., 2016, *ApJ*, 824, L19
- Ryabchikova T., Piskunov N., Pakhomov Y., Tsymbal V., Titarenko A., Sitnova T., Alexeeva S., Fossati L., Mashonkina L., 2016, *MNRAS*, 456, 1221
- Sadakane K., Jugaku J., Takada-Hidai M., 1988, *ApJ*, 325, 776
- Saito Y.-J., Takada-Hidai M., Honda S., Takeda Y., 2009, *PASJ*, 61, 549
- Seaton M. J., 1962, in Bates D. R., ed., *Atomic and Molecular Processes The Theory of Excitation and Ionization by Electron Impact*. p. 375
- Shulyak D., Tsymbal V., Ryabchikova T., Stütz C., Weiss W. W., 2004, *A&A*, 428, 993
- Sitnova T., Zhao G., Mashonkina L., Chen Y., Liu F., Pakhomov Y., Tan K., Bolte M., Alexeeva S., Grupp F., Shi J.-R., Zhang H.-W., 2015, *ApJ*, 808, 148
- Sitnova T. M., Mashonkina L. I., Ryabchikova T. A., 2016, *MNRAS*, 461, 1000
- Smith K. C., 1994, *A&A*, 291, 521
- Sneden C., Crocker D. A., 1988, *ApJ*, 335, 406
- Sneden C., Gratton R. G., Crocker D. A., 1991, *A&A*, 246, 354
- Steenbock W., Holweger H., 1984, *A&A*, 130, 319
- Takeda Y., Hashimoto O., Taguchi H., Yoshioka K., Takada-Hidai M., Saito Y., Honda S., 2005, *PASJ*, 57, 751
- Takeda Y., Omiya M., Harakawa H., Sato B., 2016, *PASJ*, 68, 81
- Tsymbal V., Ryabchikova T., Sitnova T., 2019, in Romanyuk I. I., Yakunin I. A., Kudryavtsev D. O., eds, *Physics of magnetic stars Vol. 518 of Astronomical Society of the Pacific Conference Series, Software for NLTE spectrum fitting*. p. 247
- Umeda H., Nomoto K., 2003, *Nature*, 422, 871
- van Regemorter H., 1962, *ApJ*, 136, 906
- Vladilo G., Abate C., Yin J., Cescutti G., Matteucci F., 2011, *A&A*, 530, A33
- Wolfe A. M., Gawiser E., Prochaska J. X., 2005, *ARA&A*, 43, 861
- Woolley R. D. V. R., Allen C. W., 1948, *MNRAS*, 108, 292
- Yakovleva S. A., Voronov Y. V., Belyaev A. K., 2016, *A&A*, 593, A27
- Zatsarinny O., Bartschat K., 2005, *Phys. Rev. A*, 71, 022716
- Zhao G., Mashonkina L., Yan H. L., Alexeeva S., Kobayashi

C., Pakhomov Y., Shi J. R., Sitnova T., Tan K. F., Zhang H. W., Zhang J. B., Zhou Z. M., Bolte M., Chen Y. Q., Li X., Liu F., Zhai M., 2016, ApJ, 833, 225